Journal of Marine Science and Application (2026) 25: 1364-1391
https://doi.org/10.1007/s11804-026-00843-4

RESEARCH ARTICLE

Advanced Hydrodynamic Simulation and Validation of a Torpedo-Shaped AUV

Xiangkun Wang[1], Haichuan Zhang[1], Jiayin Chen[1], Muxin Nian[1], Zaowei Li[1] and Ping Zheng[2]

Received: 12 March 2025 / Accepted: 20 November 2025
© Harbin Engineering University and Springer-Verlag GmbH Germany, part of Springer Nature 2026

Abstract

This study numerically determines hydrodynamic coefficients of a torpedo-shaped autonomous underwater vehicle (AUV) using the shear stress transport k-ω turbulence model in COMSOL Multiphysics. Linear and nonlinear coefficients are extracted via steady-state simulations (uniform linear motion, uniformly accelerated motion, and horizontal/vertical oblique cruising) and transient simulations replicating planar motion mechanism (PMM) tests with small and large amplitudes. The sliding mesh and rotating domain techniques resolve unsteady flow characteristics during dynamic maneuvers. The methodology formalizes six-degree-of-freedom motion equations, with hydrodynamic coefficients identified through regression analysis of simulated force/moment data. Experimental validation via towing-tank testing demonstrates agreement between numerical predictions and empirical measurements, particularly in capturing nonlinear hydrodynamic effects during large-amplitude PMM maneuvers. The framework maintains geometric generality for application to diverse AUV configurations. Resultant hydrodynamic databases improve the motion prediction accuracy in dynamic environments, enhance attitude control algorithm robustness, and support hull optimization through parametric drag analysis. The hydrodynamic database established significantly improves the maneuverability prediction accuracy under turbulent marine conditions.

Keywords Torpedo-shaped AUV; Hydrodynamic coefficient; SST- k-ω turbulence model; Numerical simulation; Planar motion mechanism; Sliding mesh technique; Rotating domain method; Towing-tank validation

1 Introduction

The 21st century has welcomed a new era of marine exploration, driven by technological advancements that enable systematic investigation of oceanic resources. Autonomous underwater vehicles (AUVs), distinguished by hull geometries (such as torpedo-shaped, cylindrical, or biomimetic designs) and propulsion systems (such as propeller-driven, buoyancy-driven glider, and hybrid configurations) are pivotal tools for deep-sea missions. This study examines a torpedo-shaped hybrid AUV with adjustable horizontal stabilizers positioned aft of the propeller to enhance maneuverability. This configuration significantly enhances maneuverability across military and civilian operations (Chen, 2014).

During underwater navigation, autonomous underwater vehicles (AUVs) are subjected to hydrodynamic resistance dominated by the velocity and acceleration vectors. These forces are mathematically modeled through hydrodynamic coefficients, whose accurate determination is crucial for motion control and stability. Established methodologies for hydrodynamic coefficient computation include experimental testing, analytical semi-empirical (ASE) models, and computational fluid dynamics (CFD) simulations. Experimental approaches such as towing tank tests and rotating arm trials employ force sensors for real-time hydrodynamic load measurements. While capable of delivering high-precision data, these methods are constrained by demanding experimental conditions and high operational costs (Jentzsch et al., 2021). ASE techniques suffer dual limitations: their heavy reliance on prior knowledge restricts model generalizability (Ahmed et al., 2023), while assumption-based simplified modeling fails to accu-

Article Highlights

- The research subject is a self-developed autonomous underwater vehicle (AUV) with a streamlined design and high maneuverability.
- The shear stress transport k-ω turbulence model in the finite element software COMSOL, combined with the moving mesh and rotating domain techniques, was employed to enhance the accuracy of numerical simulation results.
- A transient simulation methodology for a large-amplitude planar motion mechanism was developed to achieve high-precision determination of nonlinear hydrodynamic coefficients for the AUV, with its accuracy experimentally validated through systematic testing.
- A towing platform was independently constructed to verify the accuracy of simulation results.

✉ Haichuan Zhang
zhanghaichuan@sztu.edu.cn

[1] Ringgold standard institution, Shenzhen Technology University, Shenzhen 518118, China

[2] China Great Wall Technology Group Co., Ltd. Shenzhen 518109, China

rately characterize fluid dynamic behaviors under high Reynolds number (Re) conditions or complex flow regimes (Allotta et al., 2018). CFD-based methods, empowered by advancements in computational resources, are a cost-effective alternative for hydrodynamic coefficient prediction, with their reliability validated across various underwater vehicle configurations. Foundational work by Cavallo et al. (2004) established a theoretical framework for submarine hydrodynamics. Phillips et al. (2007) demonstrated the predictive capability of CFD through ANSYS CFX simulations of torpedo-shaped AUVs, achieving <5% error in drag and moment coefficients relative to experimental data—a benchmark case for CFD validation. Recent developments have integrated machine learning (ML) into coefficient estimation workflows (Gibson and Stilwell, 2018; Shadlaghani and Mansoorzadeh, 2016; Qin et al., 2022; Benjamin and Eric, 2005; Mohamad and Miralam, 2022; Kim et al., 2015; Hong et al., 2022; Hong et al., 2021), significantly enhancing computational efficiency and accuracy.

Addressing challenges associated with the simulation of complex flow fields, Wu et al. (2022) developed a multiphysics-coupled numerical framework for underwater towed systems, discretizing cables into elastic catenary elements with Morison equation-based hydrodynamic calculations. Through CFD-empirical data fusion, Mitra et al. (2020) quantified nonlinear effects of Re on hull resistance in sloped riverine environments.

In novel AUV configuration optimization, bio-inspired design and data-driven approaches have markedly improved the performance prediction efficiency. Lu et al. (2023) implemented CFD-based, multi-objective optimization for shark-inspired AUVs, integrating parametric modeling with surrogate models to achieve 9.1% drag reduction and 6.3% energy consumption decrease. Ahmed et al. (2024), through resistance polar curve analysis, revealed lift-drag ratio versus thrust requirement trade-offs in bow-winged AUVs. Wang et al. (2023) systematically investigated AUV configuration sensitivity to blockage effects in towing tanks, proposing correction coefficients to enhance drag prediction accuracy (Ye et al., 2024). Hussain et al. (2025), through CFD simulations, elucidated the control mechanisms of forewing-tail configurations on dynamic stability. The integration of ML with CFD has revolutionized hydrodynamic modeling paradigms: Yang et al. (2021) implemented reinforcement learning for dynamic parameter optimization, overcoming local convergence limitations of gradient-based methods; Liu et al. (2024) developed a physics-informed generative adversarial network (CFD-GAN) for rapid performance prediction in high-dimensional parameter spaces (Liu et al., 2024).

Within CFD methodologies, hydrodynamic coefficients remain classified into linear and nonlinear categories despite technological advancements. Linear hydrodynamic coefficients are conventionally derived through steady-state motion simulations, including straight-line and oblique towing tests. However, nonlinear coefficient identification requires specialized planar motion mechanism (PMM) experimental protocols (Zou and Larsson, 2013). PMM experiments are further categorized based on oscillation amplitudes into small-amplitude and large-amplitude PMM tests (Shi, 2021).

Small-amplitude PMM tests employ periodic oscillatory motions with restricted amplitudes (typically 0.01 L–0.05 L, where L denotes the characteristic length), ensuring numerical convergence while capturing primary nonlinear hydrodynamic terms. However, the limited velocity and acceleration ranges inherent in this approach restrict its applicability to low-speed submersibles or those with high geometric symmetry (Wang et al., 2024; Wang et al., 2023). Hydrodynamic models derived from small-amplitude PMM data remain sufficient for motion control applications in calm marine environments with minimal flow disturbances (Lin et al., 2022).

However, this methodology has proved inadequate for characterizing high-speed, highly maneuverable submersibles operating under complex hydrodynamic conditions. Such scenarios involve significant unsteady flow separation phenomena (Zhu et al., 2025), where pronounced inertial hydrodynamic loads and memory effects originate from asymmetric vortex structures during high-angle-of-attack maneuvers (Ma et al., 2025). To address these limitations, this study implements an improved large-amplitude PMM testing protocol through COMSOL Multiphysics simulations (Liang et al., 2022). This protocol simulates four-degree-of-freedom motions (pure sway, yaw, heave, and pitch), generating amplified velocity gradients and enhanced acceleration fields to effectively elicit nonlinear flow responses.

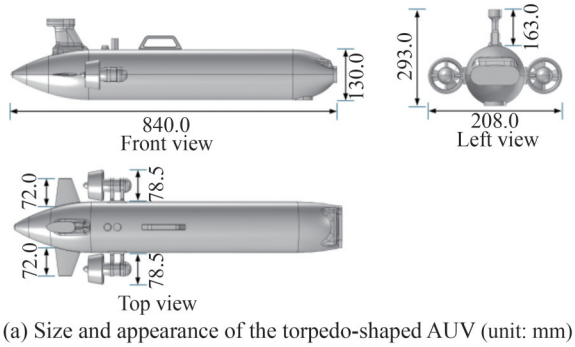
Hydrodynamic force data are obtained both through steady-state simulations (straight/oblique motions) and transient simulations (small- and large-amplitude PMM) using a sliding mesh methodology. Subsequent regression analysis of the force/moment datasets enabled the systematic extraction of dynamic coefficients. Experimental validation through a custom-built towing tank platform and dedicated test rigs confirmed the computational accuracy.

This approach facilitates the determination of higher-order hydrodynamic derivatives (e. g., quadratic damping terms and coupled inertial coefficients) essential for constructing comprehensive, six-degree-of-freedom (6-DoF), strongly nonlinear dynamic models and enhances the control law's robustness. The methodology establishes a generalized framework for predicting high-speed and high-mobility AUV motion in dynamic marine environments, exhibiting adaptability across diverse hull configurations and providing critical insights for hydrodynamic optimization of next-generation submersibles.

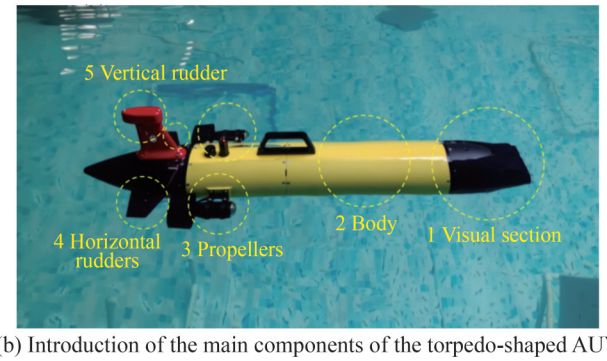
2 Model introduction

2.1 Introduction of AUV model structure

This study focuses on a torpedo-shaped AUV featuring a streamlined design. For underwater target detection, this AUV is equipped with a binocular vision system mounted on its nose cone. Two large-diameter vectored thrusters at the stern enable high-speed cruising, while adjustable horizontal control surfaces positioned aft of the propeller enhance maneuverability through vectored thrust. A vertical stabilizer mounted atop the horizontal tails improves the pitch stability. The AUV's configuration and key parameters are detailed in Figure 1 and Table 1, respectively.



(a) Size and appearance of the torpedo-shaped AUV (unit: mm)



(b) Introduction of the main components of the torpedo-shaped AUV

Figure 1 Configuration of the torpedo-shaped autonomous underwater vehicle (AUV)

Table 1 Key parameters of the torpedo-shaped autonomous underwater vehicle (AUV)

Total mass (kg)	Total gravity (N)	Total buoyancy (N)	Speed (knots)	DoF
8.3	81.3	83.5	0–3.8	3
Submerge depth (m)	Operation time (h)	Body length (mm)	Body width (mm)	Body height (mm)
100	3.5	840	208	220

2.2 Introduction of the mathematics model

Herein, the motion of the torpedo-shaped AUV is described using two coordinate systems: an Earth-fixed frame (O_E-XYZ)) and a body-fixed frame (o_b-xyz) (Figure 2).

In the body-fixed frame, the AUV's linear velocity $\boldsymbol{v}$ and angular velocity $\boldsymbol{\omega}$ are expressed as

$$\boldsymbol{v} = [\,u, v, w\,]^{\mathrm{T}} \in \mathbb{R}^3, \boldsymbol{\omega} = [\,p, q, r\,]^{\mathrm{T}} \in \mathbb{R}^3 \tag{1}$$

where $\boldsymbol{v}$ and $\boldsymbol{\omega}$ denote the linear and angular velocities relative to the selected reference frame, respectively, and $\boldsymbol{\nu} = [\,\boldsymbol{v}^{\mathrm{T}}, \boldsymbol{\omega}^{\mathrm{T}}\,]^{\mathrm{T}}$ represents the overall velocity vector of the AUV.

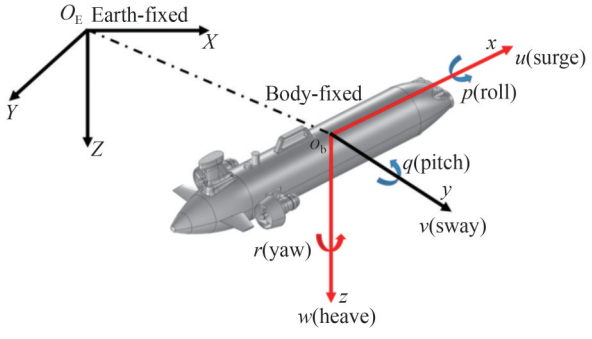


Figure 2 Reference frames of the torpedo-shaped AUV

Similarly, the position vector $\boldsymbol{\eta}_1$ and orientation vector $\boldsymbol{\eta}_2$ of the AUV with respect to the Earth-fixed frame are expressed as

$$\boldsymbol{\eta}_1 = [\,x, y, z\,]^{\mathrm{T}} \in \mathbb{R}^3, \boldsymbol{\eta}_2 = [\,\phi, \theta, \psi\,]^{\mathrm{T}} \in \mathbb{R}^3 \tag{2}$$

where $\boldsymbol{\eta}_1$ and $\boldsymbol{\eta}_2$ denote the AUV's position and attitude, respectively, and together they constitute the complete position orientation vector of the AUV, i.e., $\boldsymbol{\eta} = [\,\boldsymbol{\eta}_1^{\mathrm{T}}, \boldsymbol{\eta}_2^{\mathrm{T}}\,]^{\mathrm{T}}$

The origin of the body-fixed frame is located at the AUV's center of mass (COM), with the buoyancy center positioned such that the COM coincides with the center of buoyancy. Geometric symmetry about the xz-plane, combined with near-symmetry about xy- and yz-planes, establishes inherent hydrodynamic stability along the longitudinal (x-axis) direction. This passive stability enables autonomous recovery to equilibrium orientation without requiring external interventions, justifying the angular velocity-nullification assumption. Consequently, the equations of motion demonstrate decoupled dynamics in the heave, roll, and pitch degrees of freedom. Under these premises, the AUV's state-space dynamic model reduces to:

$$\dot{x} = u\cos\psi - v\sin\psi \tag{3(a)}$$

$$\dot{y} = u\sin\psi + v\cos\psi \tag{3(b)}$$

$$\dot{z} = w \tag{3(c)}$$

$$\dot{\psi} = r \tag{3(d)}$$

$$\dot{u} = \frac{1}{m_{11}}\left[m_{22}vr + X_u u + X_{u|u|}u|u| + \tau_X\right] \tag{3(e)}$$

$$\dot{v} = \frac{1}{m_{22}}\left[- m_{11}ur + Y_v v + Y_{v|v|}v|v|\right] \quad 3(f)$$

$$\dot{w} = \frac{1}{m_{33}}\left[(W - B) + Z_w w + Z_{w|w|}w|w| + \tau_Z\right] \quad 3(g)$$

$$\dot{r} = \frac{1}{m_{44}}\left[(m_{11} - m_{22})uv + N_r r + N_{r|r|}r|r| + \tau_N\right] \quad 3(h)$$

where $m_{11} = (m - X_{\dot{u}})$, $m_{22} = (m - Y_{\dot{u}})$, $m_{33} = (m - Z_{\dot{u}})$, and $m_{44} = (m - N_{\dot{u}})$ denote added mass components, while $X_{\dot{u}}$, $Y_{\dot{u}}$, $Z_{\dot{u}}$, and $N_{\dot{u}}$ represent hydrodynamic coefficients associated with the added mass components. Moreover, W and B denote the AUV's weight and buoyancy, respectively. The terms X_u, $X_{u|u|}$, Y_v, $Y_{v|v|}$, Z_w, $Z_{w|w|}$, N_r, and $N_{r|r|}$ denote hydrodynamic damping coefficients; τ_X and τ_Z denote control forces acting on the AUV in the X-, and Z-directions, respectively, and τ_N denotes the control moment about the Z-axis, all generated by two thrusters. The AUV's weight and buoyancy are almost identical (Table 1). Therefore, $(W - B)$ was assumed to be zero in CFD simulations.

3 Numerical calculation settings

Seven distinct motion patterns were investigated by simulating the AUV's motion in COMSOL Multiphysics®: uniform linear motion, uniformly accelerated linear motion, oblique motion, small-amplitude planar motion mechanism (PMM) horizontal motion, small-amplitude PMM vertical motion, large-amplitude PMM horizontal motion, and large-amplitude PMM vertical motion.

The SST k-ω turbulence model was employed throughout the computational process. This model was implemented using the Turbulent Flow, SST k-ω interface of the CFD Module (COMSOL, 2024a). To enhance solution convergence and computational efficiency, geometric smoothing was applied to regions with high curvature gradients, such as the tail tip and control surfaces, thereby optimizing the mesh quality. A sliding-mesh approach, implemented through the ALE moving-mesh capabilities of COMSOL Multiphysics® (version 6.2) (COMSOL, 2024b) , was employed to preserve mesh integrity during AUV displacement. This method mitigated mesh distortion originating from the compression and traction effects, thereby ensuring continuous convergence of the fluid-structure interaction solution.

Regarding the mesh generation strategy, adaptive sizing was employed based on the surface curvature. Smaller tetrahedral elements (minimum edge length: 0.000 2 m) were concentrated on high-curvature regions, including horizontal and vertical stabilizers, while larger tetrahedral elements (maximum edge length: 0.55 m) were utilized for the main cylindrical hull. A boundary layer mesh with eight prismatic layers and a stretching factor of 1.2 was implemented in accordance with COMSOL meshing guidelines (COMSOL, 2024b) to resolve near-wall flow phenomena. Far-field mesh topology varied across test cases but consistently adhered to the convergence stability and accuracy requirements. Temporal discretization was controlled via a time step of 0.1 s for steady-state motions and a refined time step of 0.02 s for unsteady maneuvers, determined through condition-specific sensitivity analyses. The nonlinear solver was allowed a maximum of 100 iterations per time step, and convergence was declared when normalized residuals of all governing equations were less than a threshold of 1×10^{-5} (COMSOL, 2024c).

All numerical simulations were conducted using the CFD Module (Fluid Flow interface) within COMSOL Multiphysics® (version 6.2). Incompressible Navier-Stokes equations were solved using the finite-element formulation implemented in COMSOL, and turbulence was simulated via the (SST) k-ω turbulence model. Solver settings, including time stepping, maximum iterations per time step, and residual tolerances, as well as numerical schemes, adhered to the description in the COMSOL Multiphysics® Reference Manual (version 6.2) (COMSOL, 2024b).

4 Methodology

4.1 Governing equations

The torpedo-shaped AUV remained completely submerged during all operational phases. Its hydrodynamic behavior was governed by incompressible Navier-Stokes equations. In three-dimensional Cartesian coordinates (x, y, z), the primitive variable form was written based on the principles of continuity and momentum conservation:

$$\frac{\partial \rho}{\partial t} + \frac{\partial (\rho u_i)}{\partial x_i} = 0 \quad (4)$$

$$\rho\left[\frac{\partial u_i}{\partial t} + \frac{\partial\left(\bar{u}_i\bar{u}_j\right)}{\partial x_j}\right] = -\frac{\partial p}{\partial x_i} + \frac{\partial}{\partial x_j}\left[\boldsymbol{\mu}\left(\frac{\partial u_i}{\partial x_j} + \frac{\partial u_j}{\partial x_i} - \frac{2}{3}\delta_{ij}\frac{\partial u_i}{\partial x_i}\right)\right] + \frac{\partial}{\partial x_j}\left(-\rho u_i' u_j'\right) \quad (5)$$

where $i, j = 1, 2, 3$; u_i and u_j are the fluid velocity components in the i and j directions, respectively; x_i denotes the spatial coordinates in the rectangular system; ρ is the fluid density; p represents pressure; t is the physical time; $\boldsymbol{\mu}$ is the dynamic viscosity; δ is the Kronecker delta; and $-\rho\bar{u}_i'\bar{u}_j'$ refers to the Reynolds stress tensor derived from the Boussinesq hypothesis (Hinze, 1975).

The SST k-ω turbulence model (Menter, 1994) was adopted to capture possible flow separation during oblique

motion and PMM maneuvers of the AUV while maintaining a balance between computational accuracy and cost. This model incorporated Wilcox's k-ω baseline closure (Wilcox, 2008) for accurate near-wall resolution of the boundary layer behavior and switched to the standard k-ε formulation (Launder and Spalding, 1974) for outer flow regions for improved numerical stability. The hybrid Reynolds-averaged Navier-Stokes (RANS) strategy provided high fidelity in the simulation of separated flows and complex geometries, delivering reliable predictions for the hydrodynamic performance of the torpedo-shaped AUV across various operating conditions.

4.2 Boundary conditions

Aiming at addressing diverse simulation scenarios herein, customized boundary conditions were implemented to enhance the solution accuracy. In steady-state numerical simulations, the AUV remained stationary while the surrounding flow field was constructed as a rectangular computational domain through relative water motion (Figure 3(a)), with L and D representing the AUV's length and hull diameter, respectively. The inlet boundary was positioned $0.5L$ ahead of the bow, employing a velocity boundary condition to define undisturbed uniform inflow with velocity vectors perpendicular to the inlet plane. The outlet boundary extended $2L$ downstream of the stern, and lateral open boundaries maintained a distance of $11D$ from the vehicle surface. By eliminating pressure gradients, these open boundaries enabled free fluid outflow, effectively suppressing boundary reflection effects on the surrounding flow field. An inlet distance of $0.5L$ ensured fully developed inflow, while an outlet extension of $2L$ sufficiently accommodated the $0.4L$ wake dissipation region, meeting the computational requirements for flow field stability.

For the dynamic simulation of PMM motions, the AUV executed prescribed movements within a stationary fluid domain, modeled as a 40 m × 15 m × 15 m computational domain with dynamic meshing (Figure 3(b)). The AUV was axially positioned $50L$ from the front boundary and $2.5L$ from the rear boundary, while lateral open boundaries were set at $57D$ to satisfy spatial demands for dynamic flow development.

All boundaries adopted open conditions, aligning with the physical mechanisms of vorticity transport during motion and adhering to grid independence criteria that required boundary distances more than thrice the characteristic dimension. Considering a cruising speed of 1 m/s and a maximum motion period of 5 s, a domain length of 40 m not only fulfilled the minimum data acquisition requirement of 25 m (corresponding to a maximum physical time spanning five cycles) but also optimized the computational efficiency through a dynamic compression mechanism in the outer region (Figure 4). This mechanism adaptively adjusted the grid density on the basis of the motion phase: the tail

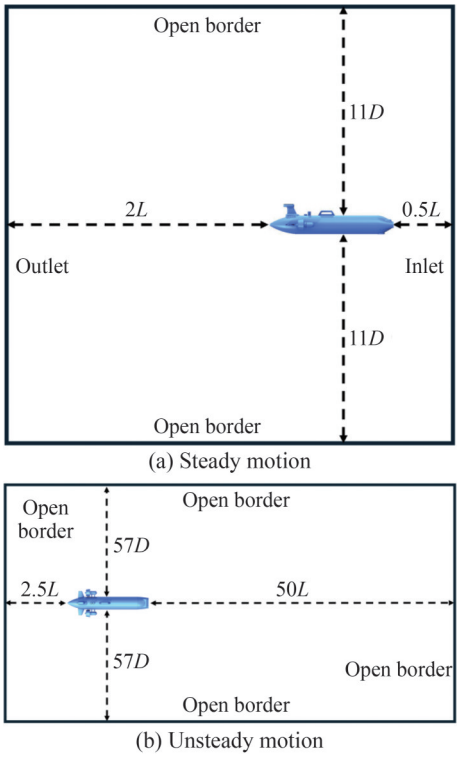


Figure 3 Boundary conditions of steady motion and unsteady motion

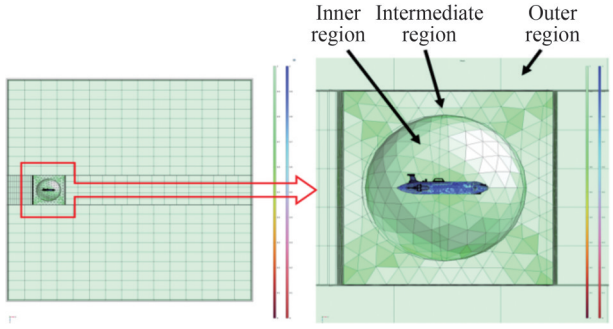


Figure 4 Meshes of three subregions during unsteady motion

region employed finer mesh refinement in the initial stages to resolve starting vortices, while the head region was refined in the final stages to capture braking flow fields. A width of 15 m minimized grid counts without compromising resolution, and a height of 15 m provided adequate oscillation space for pure heave and sway motions. The dimensions of the computational domain (length, width, and height) were sufficiently designed to ensure the submersible could freely maneuver within the central region without interference from boundary effects or numerical artifacts. Notably, 90° axial rotation of the submersible aligned the oscillation direction with the domain height for both the heave and sway modes, preserving flow symmetry and data comparability across motion configurations. Therefore, the boundary conditions and physical time settings established herein ensured both computational accuracy and a reasonable computational time.

4.3 Mesh generation

The AUV's cylindrical hull geometry allowed for simplified meshing strategies. With the exception of the horizontal stern plane's thin surfaces, the absence of geometric discontinuities such as sharp edges or protrusions enabled the use of free tetrahedral meshes. Critical stern plane regions were assigned refined elements with 0.2 m maximum size and 0.002 m minimum size, achieving an optimal balance between the solution accuracy and computational efficiency (Figure 5). All meshing operations were conducted using COMSOL Multiphysics with controlled element-growth rates.

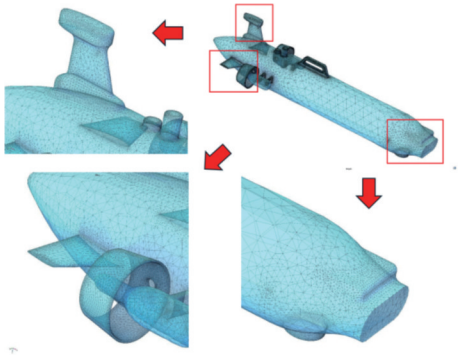


Figure 5 Meshes of the model

Domain decomposition strategies were implemented as per motion characteristics. For the rectilinear and oblique motion cases, the computational domain was partitioned into three hierarchically refined zones: 1) boundary layer regions utilizing prismatic elements with progressive stretching to resolve steep velocity gradients; 2) near-field regions employing fine, free tetrahedral elements (maximum size: 0.1 m) for moderate flow variations; 3) and far-field regions adopting coarser tetrahedral elements (maximum size: 0.275 m) for attenuated flow conditions. This multiscale meshing approach, visualized in Figure 6 through COMSOL implementations, was quantitatively validated through subsequent grid independence studies.

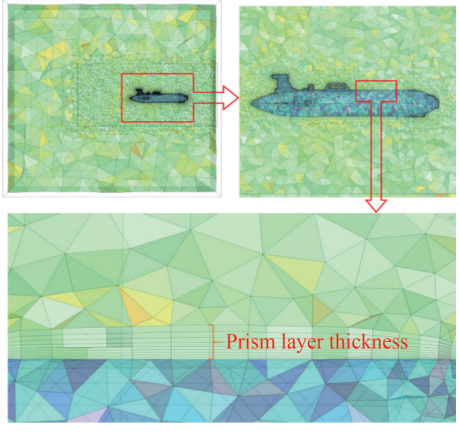


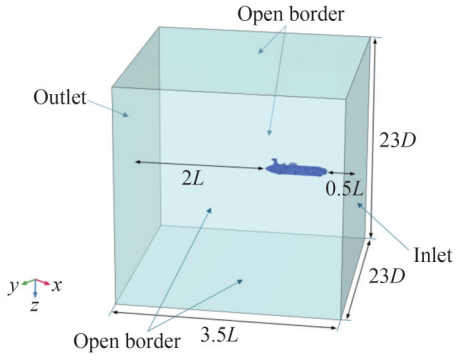
Figure 6 Meshes of three subregions during steady-state motion

In the PMM simulation, the fluid computational domain surrounding the AUV was partitioned into three dynamically coupled regions: the inner region, intermediate region, and outer region (Figure 4). The inner region was defined using the Rotating Domain capability in the Moving Mesh interface of COMSOL Multiphysics® (version 6.2) (COMSOL, 2024b), creating a spherical zone (comprising a refined unstructured tetrahedral mesh) around the AUV surface to resolve steep velocity gradients. A user-prescribed rotational axis and angular velocity enforced sinusoidal variations in heading and pitch within this region. The intermediate region, enveloping the inner region, utilized a sliding mesh technique (also via ALE-based Moving Mesh functionality) to synchronize its displacement with the AUV trajectory while maintaining stable internal mesh size and quality, thereby preventing geometric deformation–induced numerical errors. The outer region, extending beyond the intermediate region, was constructed using deformable hexahedral meshes whose boundaries dynamically adjusted mesh dimensions on the basis of the AUV's motion direction. For instance, the aft domain exhibited a higher compression ratio during the initial phase of motion, while increased compression occurred in the fore domain during the terminal phase. Coarser meshes were adopted in this region to reduce computational costs. Interfaces between adjacent domains ensured continuous transfer of flow-field variables across all regions, and mesh densities were rigorously validated through grid independence analysis detailed in subsequent sections.

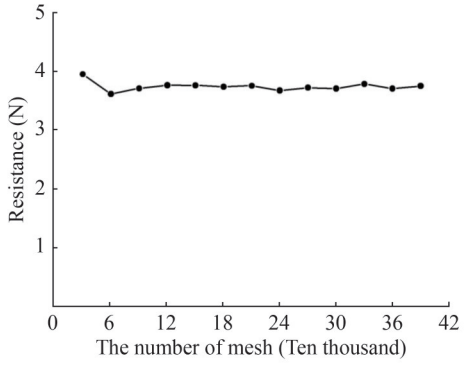
4.4 Grid independence

Mesh sensitivity analysis plays a pivotal role in balancing between computational cost and solution accuracy, as both numerical convergence and resource expenditure strongly depend on element density. This study conducted systematic grid convergence assessments through towing tests and PMM simulations. For the towing configuration (Figure 7(a)), a 3 m^3 cubic computational domain was discretized using 13 systematically refined meshes having 30 000–390 000 elements. Constant surge velocity conditions (u = 1 m/s) were applied to evaluate x-direction drag coefficient variations across mesh resolutions, establishing optimality criteria balancing between precision and computational efficiency.

As evidenced from Figure 7(b), drag force stabilization occurred at 300 000 elements with <1.5% deviation from the finest mesh configuration while reducing the computation time by 62%. The validated configuration comprised an eight-layer boundary zone with a stretching factor of 1.2, transitioning to graded tetrahedral elements in the near-field (0.001–0.100 m sizing) and coarse tetrahedral elements in the far-field (0.020–0.275 m sizing). This hierarchical meshing strategy captured 92.3% of velocity gradient features while achieving 41% faster convergence than baseline con-



(a) Computational fluid domain around the AUV during steady-state motion



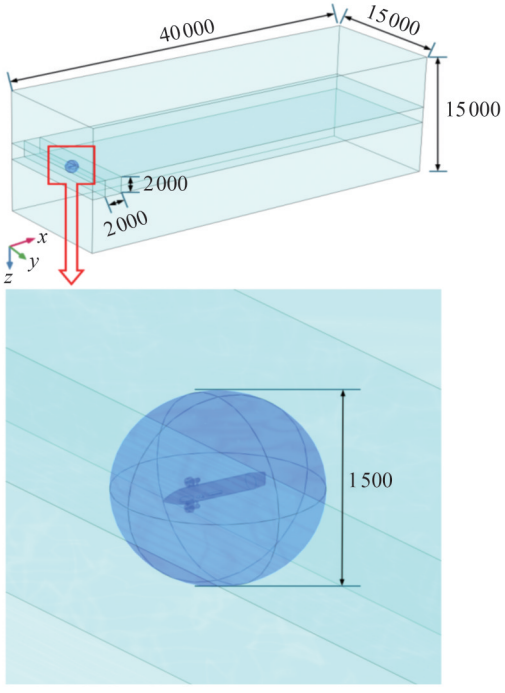
(b) Drag force of the AUV in the *x*-direction versus the number of meshes

Figure 7 Computational fluid domain around the AUV during steady-state motion and drag force of the AUV in the *x*-direction versus the number of meshes

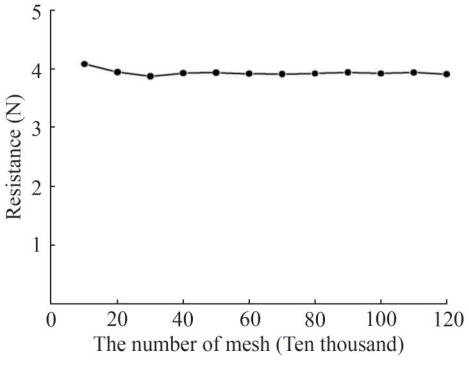
figurations, exhibiting an effective balance between flow physics resolution and computational practicality.

The PMM simulation framework employed a stratified computational domain measuring 45 m (length) × 15 m (width) × 15 m (height) (Figure 8(a)). Three dynamically adaptive meshing zones were implemented to address motion kinematics: 1) the innermost spherical rotational domain with 0.75 m radius surrounding the AUV, employing ultrafine tetrahedral elements (0.000 2–0.100 0 m sizing) to resolve vorticity fields during prescribed sinusoidal pitching cycles (amplitude: 0.04 m; angular frequency: 0.4π rad/s); 2) encapsulating this core, a 2 m^3 cubic sliding interface zone utilized graded tetrahedral meshes (0.002–0.200 m) with real-time topology adaptation algorithms, dynamically adjusting the element connectivity to track trajectory-induced deformations; 3) the outermost domain transitioned to structured hexahedral elements with dynamic sizing (0.05–0.50 m), automatically scaling on the basis of local velocity gradient magnitudes.

Systematic mesh sensitivity analysis evaluated 12 configurations spanning from 100 000 to 1.2 million elements at steady longitudinal flow (V = 1 m/s). Monitoring of *x*-direction drag coefficients revealed solution convergence at 900 000 elements, showing <2% deviation from the finest mesh configuration while reducing the computational time by 58%. The optimized meshing strategy comprised isotropic refinement in the rotational core (Jacobian > 0.3), anisotropic tetrahedral morphing in the dynamic interface (skewness < 0.7), and adaptive hexahedral elements in the far field (growth rate: 1.18). This multilayered approach resolved 94.6% of pressure fluctuation spectra while maintaining the temporal resolution to be <0.008 s for vortex shedding events, achieving an optimal equilibrium between hydrodynamic fidelity and computational efficiency (Figure 8(b)).



(a) Computational fluid domain around the AUV during unsteady motion (unit:mm)



(b) Average drag force on the AUV in the *x*-direction versus the number of meshes

Figure 8 Computational fluid domain around the AUV during unsteady motion and average drag force on the AUV in the *x*-direction versus the number of meshes

4.5 Grid convergence verification and richardson extrapolation

In numerical simulations, in particular those relating to fluid dynamics, grid refinement can significantly affect the

accuracy of results. Aiming at ensuring the accuracy of numerical solutions, this study employed Richardson extrapolation to verify grid convergence (Roache, 1998), following the procedures and mesh handling functionalities described in the COMSOL Multiphysics® Reference Manual (version 6.2) (COMSOL, 2024b). Simulations were conducted for two test cases: straight-line motion and PMM motion. For the straight-line motion case, the AUV moved at a constant speed of 1 m/s along the *x*-axis; for the PMM case, the AUV underwent a PMM motion with 0.04 m amplitude and 0.4π rad/s frequency. In both cases, coarse and fine grids were used for simulations.

Coarse and fine grid resolutions were selected for the grid configuration: a coarse grid with a minimum element size of h_{coarse} and a fine grid with a minimum element size of h_{fine}. Using these grid resolutions, the drag force along the *x*-axis acting on the AUV was calculated, and the corresponding drag coefficient was determined as follows:

$$C_{\text{d}} = \frac{F_{\text{d}}}{\frac{1}{2}\rho v^2 A_{\text{proj}}} \tag{6}$$

where F_{d} denotes the drag force acting on the AUV along the *x*-direction; ρ is the fluid density, assumed to be 1 000 kg/m^3 for water; v is the velocity of the AUV relative to the flow, assumed to be 1 m/s; and A_{proj} is the reference area, defined as the maximum frontal projected area of the object. Herein, A_{proj} included the hull, the thruster, and the rudder surfaces, with a value of 0.02 m^2.

In the "steady-speed, straight-line motion" case, the minimum element size for the coarse grid was selected as h_{coarse} = 0.003 5 m, with the corresponding drag force $F_{\text{d}}^{\text{coarse}}$ acting on the AUV being 3.85 N. The minimum element size for the fine grid was h_{fine}=0.001 m, and the corresponding drag force $F_{\text{d}}^{\text{fine}}$ was 3.79 N. Using the drag force calculation formula, the drag coefficient for the coarse grid, $C_{\text{d}}^{\text{coarse}}$, was calculated to be 0.385, while the drag coefficient for the fine grid, $C_{\text{d}}^{\text{fine}}$, it is calculated to be 0.379. Richardson extrapolation was then applied to estimate the theoretical drag coefficient for an infinitely refined grid. The following is the basic formula for Richardson extrapolation:

$$C_{\text{d}}^{\infty} = \frac{4C_{\text{d}}^{\text{fine}} - C_{\text{d}}^{\text{coarse}}}{3} \tag{7}$$

By substituting the drag coefficients of coarse and fine grids into Equation (7), an extrapolated value of 0.377 was obtained, which closely matched the result from the fine grid calculation, i.e., the theoretical drag coefficient for an infinitely refined grid, C_{d}^{∞}, was almost equal to $C_{\text{d}}^{\text{fine}}$, with a difference of only 0.5%. This indicated that the numerical solution had converged and that the fine grid had been sufficiently refined.

In the PMM motion case, the minimum element size for the coarse grid was set to h_{coarse} = 0.001 m, resulting in a drag force $F_{\text{d}}^{\text{coarse}}$ of 4.01 N on the AUV. For the fine grid, the minimum element size was h_{fine} = 0.000 2 m, with the corresponding drag force $F_{\text{d}}^{\text{fine}}$ being 3.94 N. Using the abovementioned drag coefficient formula, the $C_{\text{d}}^{\text{coarse}}$ value was calculated to be 0.401, while the $C_{\text{d}}^{\text{fine}}$ value was calculated to be 0.394. Applying Richardson extrapolation, the C_{d}^{∞} value was estimated to be 0.392.

The extrapolated value closely matched the result obtained from the fine grid configuration, with a difference of only 0.5%, indicating that the numerical solution had converged. This further confirmed the validity of the grid refinement.

Based on the computations and verification presented, it can be concluded that the grid resolution selected exerted a minimal impact on results. The fine grid was sufficiently refined, and further refinement did not significantly improve the accuracy. Moreover, Richardson extrapolation was proved to be an effective method for assessing the convergence of the numerical solution, ensuring the reliability of simulation results.

4.6 Principles of hydrodynamic force computation

Herein, hydrodynamic forces (including drag and moment) acting on the AUV were computed by integrating the stresses exerted by the fluid on the AUV surface. We used the CFD module within COMSOL Multiphysics® (version 6.2), combined with incompressible Navier-Stokes equations, to simulate the interaction between the fluid and AUV. Navier-Stokes equations described the conservation of momentum in the fluid, and we assumed the fluid was incompressible, meaning its density was constant.

In the simulation, a no-slip boundary condition was applied to the AUV surface, meaning the fluid velocity at the surface was zero. This created a significant velocity gradient between the fluid and the solid surface, particularly in the boundary layer region near the AUV. Aiming at accurately capturing these details, especially in the boundary layer region, we employed boundary-layer meshing to resolve the flow behavior near the wall. The meshing strategy is detailed in Section 4.3.

Navier-Stokes equations were solved using the CFD module with the finite element method, obtaining the velocity and pressure at each mesh node. The computed pressure field p and viscous stress field $\boldsymbol{\tau}$ were then used to calculate forces acting on the AUV surface. The surface traction force was formed by the fluid pressure and shear contributions and was expressed as

$$\boldsymbol{t} = -p\boldsymbol{n} + \boldsymbol{\tau} \cdot \boldsymbol{n} \tag{8}$$

where $\boldsymbol{t}$ denotes the traction force, p is the local pressure in the fluid, $\boldsymbol{\tau}$ is the viscous stress tensor, and $\boldsymbol{n}$ is the unit

normal vector on the AUV surface. $\boldsymbol{\tau}$ was related to the velocity gradient in the fluid:

$$\boldsymbol{\tau} = \mu(\nabla \boldsymbol{u} + \nabla \boldsymbol{u}^{\mathrm{T}}) \tag{9}$$

where μ denotes the dynamic viscosity, and $\boldsymbol{u}$ is the fluid velocity field.

After obtaining the pressure and viscous stress at each mesh node, we employed surface integration to compute the total hydrodynamic force $\boldsymbol{F}$ and moment $\boldsymbol{M}$ on the AUV surface:

$$\boldsymbol{F} = \int_S (-p\boldsymbol{n} + \boldsymbol{\tau} \cdot \boldsymbol{n}) \mathrm{d}S \tag{10}$$

$$\boldsymbol{M} = \int_S \boldsymbol{r} \times \boldsymbol{t} \mathrm{d}S \tag{11}$$

where $\boldsymbol{r}$ denotes the position vector from a reference point (such as the COM) to the surface element and $\boldsymbol{t}$ denotes the traction force. By integrating the traction across the entire AUV surface, we computed the total drag (e.g., the drag in the forward direction $\boldsymbol{F}_x$), along with the corresponding moment.

For example, to calculate the drag force in the x-direction, $\boldsymbol{F}_x$, we integrated the x-component of the traction on the AUV surface:

$$\boldsymbol{F}_x = \mathrm{intop}_1(\mathrm{spf.T_stress}x) \tag{12}$$

$$\mathrm{spf.T_stress}x = -p \cdot \boldsymbol{n}x + \mathrm{spf.K_stress}x \tag{13}$$

where intop_1 denotes the surface integral operator in COMSOL, while spf.T_stress$x$ and spf.K_stress$x$ denote the traction and viscous forces, respectively, acting in the x-direction at each point on the AUV surface. Moreover, p denotes the fluid pressure, and $\boldsymbol{n}x$ is the x-component of the unit normal vector (for more details on the symbols, variable names, and calculation methods, please refer to manuals). Through this integration, we could calculate the value of $\boldsymbol{F}_x$. The moments were calculated following a similar approach, integrating the traction and combining it with the moment arm.

In COMSOL, these calculations were performed using the Fluid Flow Interface and the Navier-Stokes Solver. The pressure, velocity, and stress values for each computational element were extracted using the postprocessing module, and numerical integration was performed using built-in integration operators to obtain forces and moments. For transient conditions (e.g., PMM motion), surface forces were recorded at each time step, followed by time history analysis to calculate hydrodynamic coefficients. This procedure is detailed in Section 5. Furthermore, we ignored the effects of gravity and buoyancy during the calculation, as the weight and buoyancy of the AUV were approximately equal and opposite, effectively eliminating each other (Section 2.2). Therefore, the final hydrodynamic forces computed accounted for only fluid forces on the AUV. To ensure the accuracy of results, particularly in boundary layer regions, the mesh was refined and grid independence verified via grid convergence verification (Section 4.5). This process ensured that results were independent of the mesh resolution and time step.

5 CFD simulation

This study developed protocols for identifying hydrodynamic coefficients via systematic numerical simulation, covering steady-state and unsteady motion regimes. Steady-state analyses encompassed fundamental modes including uniform linear motion, uniformly accelerated linear motion, and oblique motion in both the horizontal and vertical planes. Unsteady hydrodynamic characterization employed PMM testing across various amplitude ranges within the horizontal and vertical planes, enabling comprehensive quantification of nonlinear damping effects and coupled dynamic responses.

5.1 Solver mode selection

The choice between steady-state and unsteady solution approaches needs to be tailored to the dynamic characteristics of the motion. For steady-state motions such as uniform rectilinear navigation and horizontal/vertical oblique towing, hydrodynamic forces and moments acting on the submersible solely depend on spatial attitude parameters (e.g., angle of attack and drift angle) and inflow conditions, exhibiting no explicit time dependency owing to constant motion states. Such problems can be efficiently addressed through steady-state methods: by establishing a steady-state flow field model in an inertial reference frame, the AUV is equivalently regarded as a stationary body with uniform inflow velocity imposed at the domain inlet. Hydrodynamic loads stabilize when the flow field converges to the steady state, enabling direct extraction of force/moment coefficients via steady-state solvers, thereby significantly reducing computational cost.

In contrast, unsteady motions such as uniformly accelerated linear motion and those generated during PMM tests with small/large amplitudes necessitate the use of transient methods to resolve dynamic characteristics. These motions involve time-dependent evolution of the velocity, acceleration, and attitude parameters, resulting in complex temporal variations in hydrodynamic loads—for instance, nonlinear resistance growth proportional to the square of the velocity in accelerated motion, or phase lag phenomena between inertial and damping forces during PMM oscillations. Transient methods employ time-discretization strategies (e.g., implicit time integration schemes) to iteratively solve the unsteady Navier-Stokes equations at each time

step. This allows accurate capture of unsteady flow phenomena, including vortex shedding and boundary layer evolution, thereby yielding force and moment time histories with high spatial and temporal resolution; these data are crucial for determining dynamic hydrodynamic derivatives such as the inertial and rotary terms.

5.2 Numerical simulation of steady-state motion

Steady-state motion of an AUV primarily includes straight-line motion and oblique motion.

The straight-line motion comprises uniform linear motion and uniformly accelerated linear motion. During operational deployment, an AUV typically accelerates uniformly from rest 0 m/s to a target velocity. Throughout this acceleration phase, the hydrodynamic resistance $\boldsymbol{F}_x$ acting on the AUV is governed by both instantaneous surge velocity u and surge acceleration $\dot{u}$. Straight-line motion simulations are segregated into uniform and uniformly accelerated regimes to address this coupling effect, facilitating the determination of the acceleration coefficients $X_{\dot{u}}$ and X_{uu}.

The oblique motion is further classified into horizontal plane oblique motion and vertical plane oblique motion. These regimes enable a comprehensive analysis of multi-axis hydrodynamic interactions during complex maneuvers.

5.2.1 Uniform linear motion

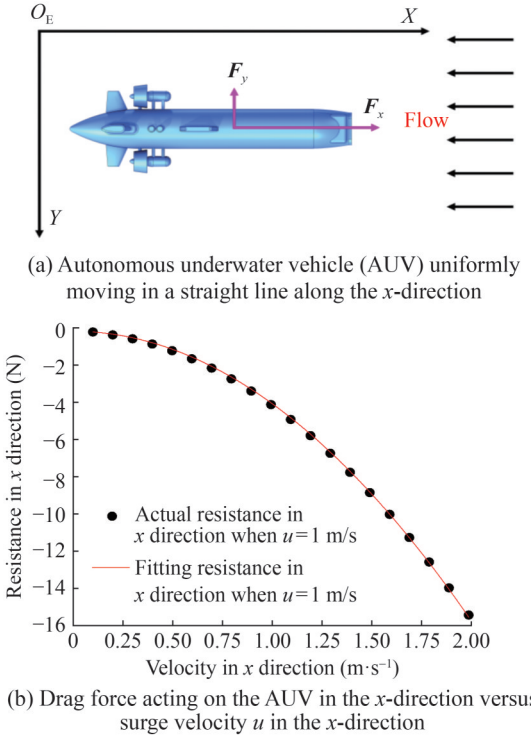
During simulations of uniform linear motion, the AUV was positioned within a cubic computational domain with an edge length of 3 m (Figure 7(a)). Domain boundaries, excluding the inlet and outlet, were configured as open-channel flow conditions to eliminate wall interference effects, enabling fluid to freely exit without flow recirculation. $\boldsymbol{F}_x$ and $\boldsymbol{F}_y$ were defined as hydrodynamic drag forces along the longitudinal and transverse axes, respectively, corresponding to the surge and sway directions.

Figure 9(a) shows the simulation setup for longitudinal motion, where the AUV remains stationary while uniform inflow velocities are imposed at the domain inlet. To replicate the operational surge velocity range of the AUV (maximum speed: 2 m/s), 20 simulation cases were executed with inlet velocities being incremented from 0.1 to 2.0 m/s in 0.1 m/s steps. Steady-state solutions were computed for each case to quantify the surge-direction drag force $\boldsymbol{F}_x$. The longitudinal hydrodynamic force $\boldsymbol{F}_x$ of the AUV can be expressed as

$$\boldsymbol{F}_x = X_{uu}u^2 \tag{14}$$

where the surge resistance $\boldsymbol{F}_x$ represents the drag force acting on the AUV along the x-direction during straight-line motion; X_{uu} is the hydrodynamic coefficient of the AUV along the x direction; u represents the AUV's surge velocity relative to the flow. Water density ρ = 1 000 kg/m^3 and characteristic length L=0.84 m have been adopted as reference parameters.

Post-convergence hydrodynamic drag forces and velocity profiles were quantified. The COMSOL Multiphysics fitting module was employed to perform least squares regression on the dataset, yielding the hydrodynamic coefficient X_{uu}. The functional relationship between the $\boldsymbol{F}_x$ value and surge velocity u is shown in Figure 9(b).



(a) Autonomous underwater vehicle (AUV) uniformly moving in a straight line along the x-direction

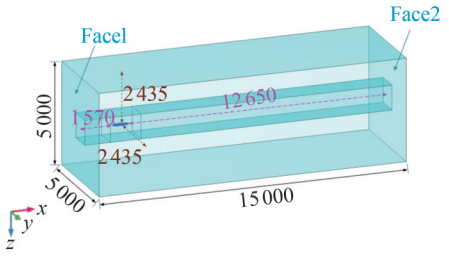
(b) Drag force acting on the AUV in the x-direction versus surge velocity u in the x-direction

Figure 9 Autonomous underwater vehicle (AUV) uniformly moving in a straight line along the x-direction and drag force acting on the AUV in the x-direction versus surge velocity u in the x-direction

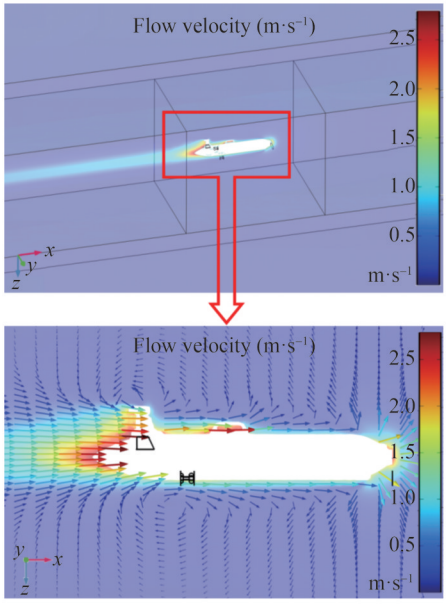
5.2.2 Uniformly accelerated linear motion

The AUV was positioned within a stationary rectangular fluid domain measuring 15 m × 5 m × 5 m. As shown in Figure 10(a), the vehicle remained stationary at the initial time step, with a clearance of 1.57 m from Surface 1, 12.65 m from Surface 2, and 2.435 m from surrounding boundaries. Simulations were conducted for uniformly accelerated linear motion with surge accelerations ranging from 0.2 m/s^2 to 1.2 m/s^2 in increments of 0.2 m/s^2, totaling six cases. Each simulation spanned a 10 s acceleration phase, with hydrodynamic forces sampled at 0.1 s intervals. Figure 10(b) shows the flow field during operation, highlighting the symmetrical flow patterns attributed to the AUV's lateral and approximate vertical symmetry. Figure 10(c) shows the distribution of the vorticity field during operation. This symmetry confined significant hydrodynamic interactions to the surge direction, resulting in the drag force $\boldsymbol{F}_x$ being described as

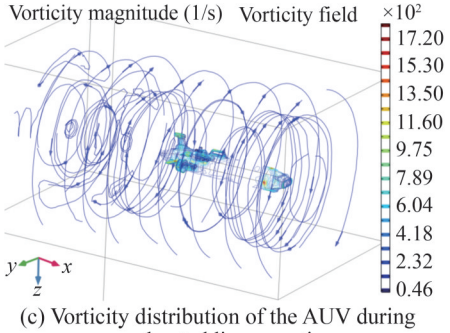
$$\boldsymbol{F}_x = X_{\dot{u}}\dot{u} + X_{uu}u^2 \tag{15}$$



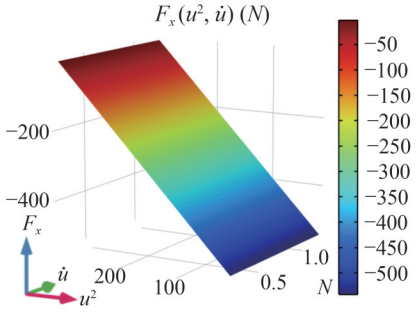
(a) Computational fluid domain around the AUV in a stationary state (unit: mm)



(b) Flow field diagram of the AUV during accelerated linear motion along the x-direction



(c) Vorticity distribution of the AUV during accelerated linear motion



(d) Drag force acting on the AUV in the x-direction versus u^2 and $\dot{u}$

Figure 10 Hydrodynamic characteristics of the AUV in a stationary state and during x-direction acceleration

The longitudinal hydrodynamic force $\boldsymbol{F}_x$ acting on the AUV was quantified through numerical simulations. Figure 10(d) shows the relationship between $\boldsymbol{F}_x$ and the u^2 and $\dot{u}$ profiles. These datasets were processed using the Least-Squares Fit function in COMSOL Multiphysics® (version 6.2) (COMSOL, 2024d), enabling the direct estimation of parameters from simulation outputs. Thereby, the hydrodynamic coefficients $X_{\dot{u}}$ and X_{uu} were obtained through a streamlined post-processing workflow via the Curve Fitting study node.

5.3 Oblique motion

Oblique motion represents planar motion of an AUV, and it is classified into horizontal and vertical plane regimes (Figure 11). The resultant velocity of the AUV in these regimes is denoted by U. Horizontal plane oblique motion involves rotating the AUV about the z-direction (vertical direction) to induce a yaw angle φ, while vertical plane oblique motion entails rotation about the y-direction (transverse direction) to establish a pitch angle θ. These angular displacements govern the coupling between the surge-sway (horizontal plane) and surge-heave (vertical plane) hydrodynamic interactions during maneuvering.

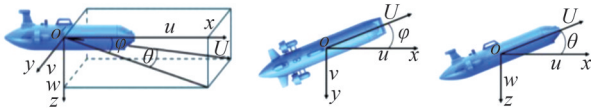


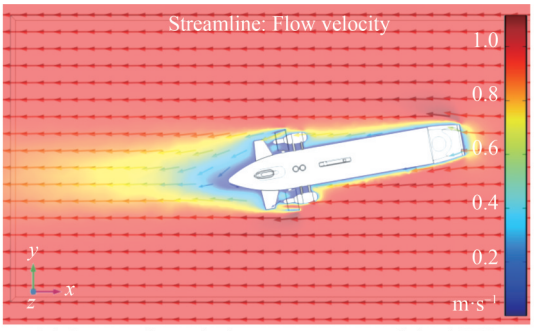
Figure 11 Hydrodynamic angles of the AUV (left), their oblique motion in the horizontal plane (middle), and their oblique motion in the vertical plane

5.3.1 Horizontal plane oblique motion

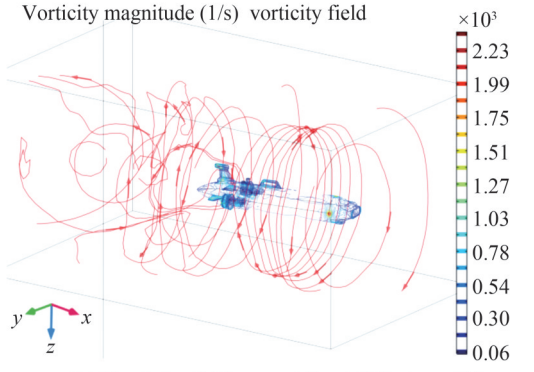
Assuming the AUV advances along the x-direction at a surge velocity of u = 1 m/s, lateral velocities v were induced by varying the yaw angle φ from 0° to 10° in 2° increments, resulting in six distinct operational regimes. Figure 12(a) and 12(b) show the flow field and vorticity field at φ = 10°. Because of the AUV's port-starboard symmetry, the sway force Y and yaw moment N exhibited antisymmetric responses to positive and negative yaw angles. The following are simplified hydrodynamic equations governing these forces and moments:

$$\begin{cases} Y = Y_v v + Y_{v|v|} v|v| \\ N = N_v v + N_{v|v|} v|v| \end{cases} \tag{16}$$

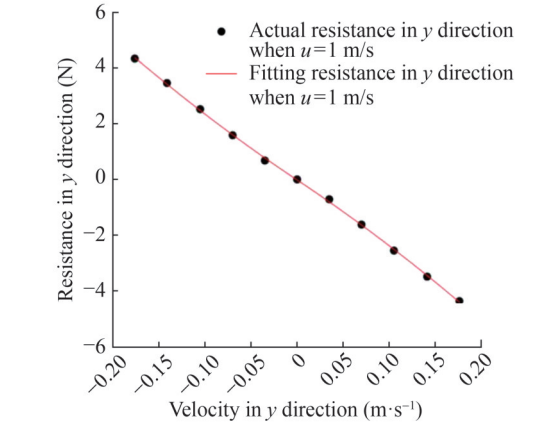
Five hydrodynamic derivatives, i. e., Y_v, $Y_{v|v|}$, $Y_{v|v|}$, N_v, and $N_{v|v|}$, were quantified through numerical simulations by employing the SST k-ω turbulence model in COMSOL Multiphysics. Flow field data were regressed using the software's least squares fitting module to extract these coefficients. The fitted curves of Y and N of the AUV as functions of sway velocity v are shown in Figures 12(c) and 12(d).



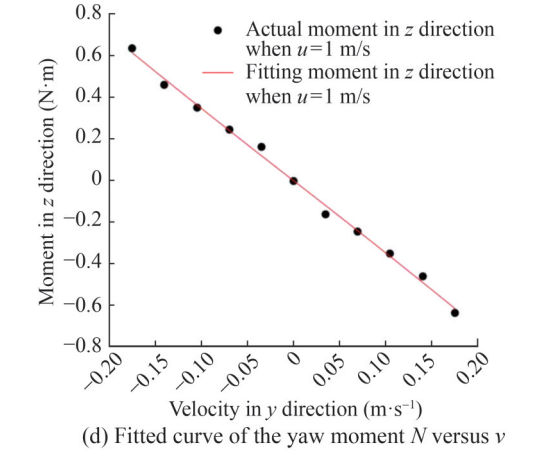
(a) Streamwise velocity contours around the AUV at yaw angle $\varphi = 10°$



(b) Vorticity field around the AUV at $\varphi = 10°$



(c) Fitted curve of the sway force Y versus sway velocity v



(d) Fitted curve of the yaw moment N versus v

Figure 12 Flow field characteristics around the AUV and fitted hydrodynamic curves for the AUV at a yaw angle of 10°

5.3.2 Vertical plane oblique motion

By varying the pitch angle θ from $-10°$ to $10°$ in $2°$ increments, vertical velocities w were induced while maintaining a constant surge velocity (u = 1 m/s). The heave force Z and pitch moment M were computed for each angular configuration. Figures 13(a) and 13(b) show the flow field and vorticity field at $\theta = 10°$, revealing asymmetric pressure distributions due to the AUV's nonsymmetrical hull form in the vertical plane. To account for this asymmetry, the constant terms Z_0 and M_0 were introduced into the hydrodynamic equations:

$$\begin{cases} Z = Z_0 + Z_w w + Z_{w|w|} w|w| \\ M = M_0 + M_w w + M_{w|w|} w|w| \end{cases} \tag{17}$$

Through data fitting, six hydrodynamic coefficients, i.e., Z_0, Z_w, $Z_{w|w|}$, M_0, M_w, and $M_{w|w|}$, could be measured. The fitted curves of the force Z and moment M of the AUV with the change in velocity w are shown in Figures 13(c) and 13(d).

5.4 Numerical simulation of unsteady motion

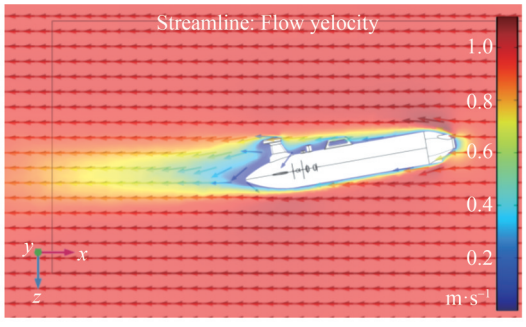
Steady-state motion simulations cannot capture nonlinear hydrodynamic coefficients, which require modeling of unsteady motion via the PMM. Based on the 6-DoF hydrodynamic principles of AUVs, PMM tests encompassed four motion regimes in the horizontal plane: small- and large-amplitude pure sway and small- and large-amplitude pure yaw. Similarly, vertical plane tests included small- and large-amplitude pure heave and pitch motions. These eight operational regimes were simulated using sliding mesh techniques, with the AUV's surge velocity maintained at u = 1 m/s.

Small-amplitude PMM tests with an oscillation amplitude of 0.04 m isolated linear hydrodynamic coefficients through harmonic oscillation analysis. Conversely, large-amplitude PMM tests with 0.3 m amplitude quantified nonlinear coefficients while validating the linear coefficient accuracy obtained from small-amplitude data. A fixed time step of 0.02 s ensured temporal resolution of the force and moment histories.

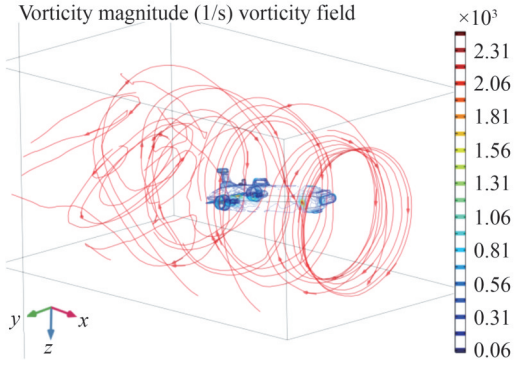
For the small-amplitude test, the period T ranged from 1 to 5 s with an interval of 0.5 s, resulting in nine cases. For the large-amplitude motion, T ranged from 5 to 10 s, also resulting in nine cases using the same sampling criteria.

5.4.1 Grid method

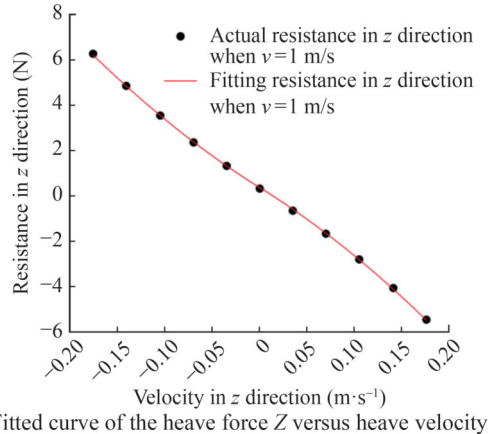
To simulate the unsteady motion of the AUV during PMM tests, multiple computational domains with distinct mesh strategies were implemented around the AUV. Given the time-dependent variations in the yaw and pitch angles, a rotating reference frame method was applied to the innermost domain adjacent to the AUV hull. This approach



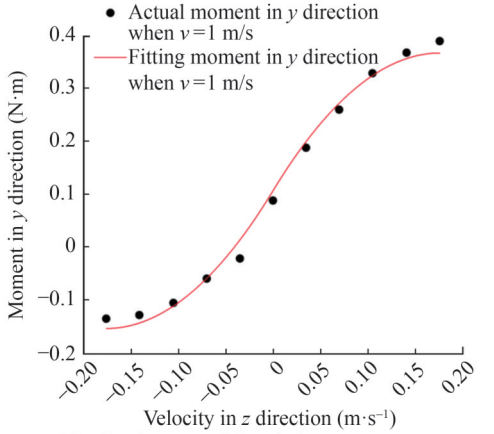
(a) Streamwise velocity contours around the AUV at pitch angle $\varphi = 10°$



(b) Vorticity field around the AUV at $\varphi = 10°$



(c) Fitted curve of the heave force Z versus heave velocity w



(d) Fitted curve of the pitch moment M versus w

Figure 13 Flow field characteristics around the AUV and fitted hydrodynamic curves for the AUV at a pitch angle of 10°

enabled rigid-body rotation of the mesh about specified axes while preserving grid orthogonality and cell quality throughout the motion, thereby ensuring numerical accuracy.

Because the AUV maintained a constant surge velocity of u = 1 m/s along the x-direction during simulation, a sliding mesh technique was used to govern the outer domain. This method permitted prescribed translational motion of the mesh at constant or accelerated velocities. Herein, the outer mesh was uniformly translated along the x-direction at 1 m/s while vertically oscillating along the y-direction with a time-dependent sway velocity v. The oscillation amplitude and angular frequency were tailored to specific test conditions.

For the outermost static domain, we employed hexahedral elements that dynamically adapted their dimensions through mesh deformation algorithms, maintaining constant cell counts despite expansion or contraction induced by inner domain motions. Figure 14 shows this multidomain mesh architecture.

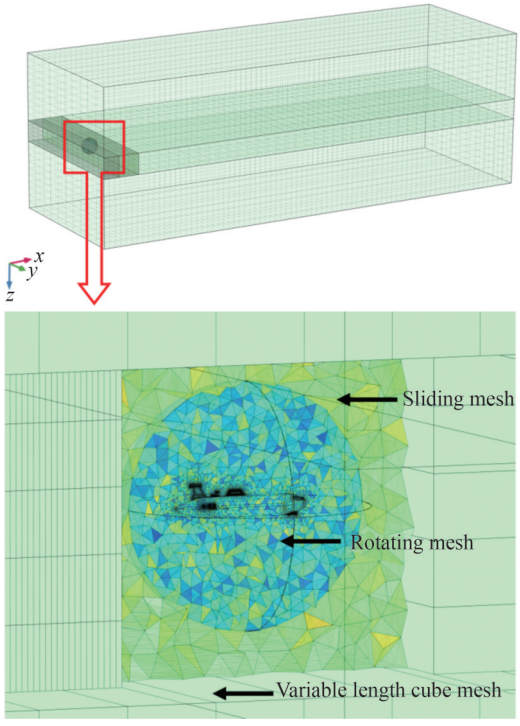


Figure 14 Meshes of three subregions in the PMM test motion simulations

5.4.2 Frequency selection

Herein, the selection of higher oscillation frequencies for transient hydrodynamic analysis was fundamentally motivated by enhancing the identifiability of hydrodynamic coefficients through the excitation of unsteady flow characteristics during the AUV's motion. Specifically, when the submersible executed pure sway, yaw, heave, and pitch motions, its hydrodynamic response inherently involved coupled effects of inertial and damping forces. By imple-

menting graded oscillation periods from 1 to 5 s (corresponding to 0.2–1.0 Hz frequency range), this approach not only covered the characteristic frequency spectrum of typical submersible maneuvering conditions but also, more critically, increased the angular frequency $\boldsymbol{\omega}$ (e. g., $\boldsymbol{\omega}$ = 2π rad/s at T = 1 s) to significantly amplify acceleration amplitudes in the motion direction (calculated as $a = \boldsymbol{\omega}^2 A$, where A denotes preset amplitude). This acceleration intensification substantially enhanced the proportional contribution of added mass forces (proportional to acceleration) to total hydrodynamic loads, thereby enabling clearer separation between inertial force coefficients and viscous damping force coefficients in CFD transient results. For instance, in pitch motion, high-frequency oscillations excited stronger trailing vortex shedding effects, while low-frequency motions tended to be dominated by quasisteady lift forces. Comparative analysis of multifrequency samples effectively differentiated the contributions of hydrodynamic coefficients from distinct flow regimes.

Regarding the numerical methodology, this study employed the SST k-ω turbulence model coupled with dynamic mesh techniques. The hydrodynamic coefficients identified were validated against physical experiments, showing <10% relative error between the coefficient $Z_{\dot{q}}$ and CFD predictions, thereby confirming the efficacy of the high-frequency oscillation analysis strategy. This "broad frequency domain" sampling approach essentially constructed hydrodynamic coefficient equations through systematic variation in flow field excitation characteristics, effectively mitigating parameter overfitting risks associated with single-frequency datasets.

5.4.3 Sampling interval effects

The selection of the sampling interval constitutes a crucial parameter influencing the precision of PMM experimental data. In transient simulations, the sampling interval directly governs the temporal discretization resolution: smaller sampling intervals enhance the capture of transient flow features induced by AUV motion through increased computational steps per unit time, thereby improving hydrodynamic coefficient accuracy at the expense of significantly elevated computational resource consumption. Conversely, larger sampling intervals reduce computational costs but risk introducing numerical noise due to insufficient temporal resolution, potentially resulting in phase distortion and amplitude errors in hydrodynamic signals.

To systematically investigate the effects of sampling interval, this study focused on pure heave motion with the following parameter combinations: amplitude A = 0.3 m, oscillation period T = 1 s, and forward velocity V = 1 m/s . These parameters were selected to maximize the sensitivity to resistance variations along the oscillation direction through large-amplitude, high-frequency excitation. Ten sampling interval configurations, ranging from 0.01 to 0.10 s (0.01 s increment), were compared using 3 s duration simulations. The precision-efficiency trade-off was evaluated by quantifying both the hydrodynamic response signal quality (characterized by the mean squared error (MSE)) and computational time consumption. The MSE was defined as $\mathrm{MSE} = \frac{1}{n}\sum_{i=1}^{n}\left(y_{\mathrm{measured},i} - y_{\mathrm{reference},i}\right)^2$, where y_{measured} denotes the measured signal, $y_{\mathrm{reference}}$ is the reference signal, and n is the number of sampling points. Figures 15(a)–(c) show resistance curves along the oscillation direction at sampling intervals of 0.10, 0.06, and 0.02 s. Smaller sampling intervals (e. g., 0.02 s) exhibited enhanced curve smoothness and effective suppression of high-frequency noise. Figures 16(a) and 16(b) show the trends of MSE and computational time as functions of the sampling interval. The MSE monotonically increased with the sampling interval owing to reduced signal resolution, while the computational time decreased with increasing sampling intervals. Cross-analysis revealed that a 0.02 s sampling interval resulted in an optimal balance: the system maintained a low MSE while ensuring reasonable computational efficiency. This result validated the effectiveness of the parameter in reconciling the measurement accuracy with operational efficiency.

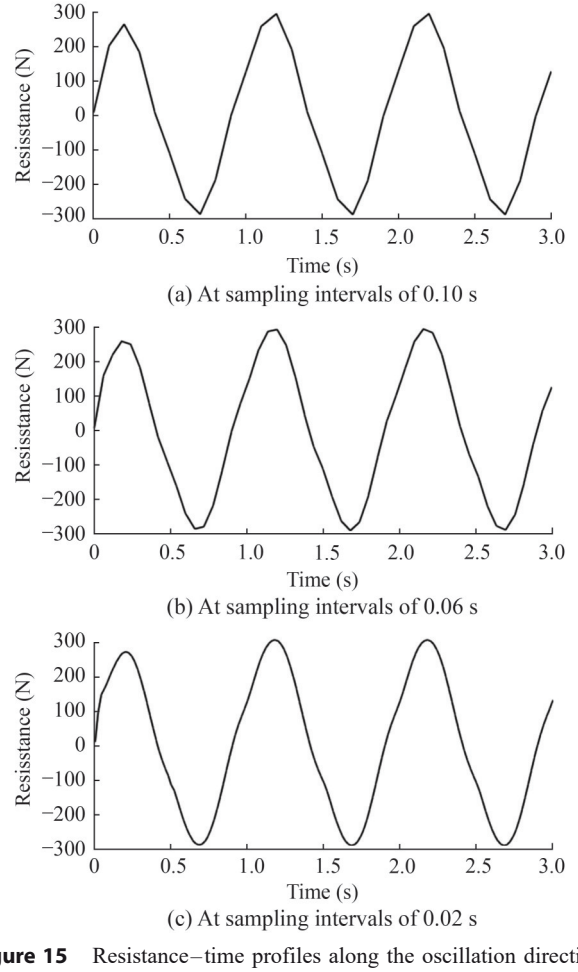
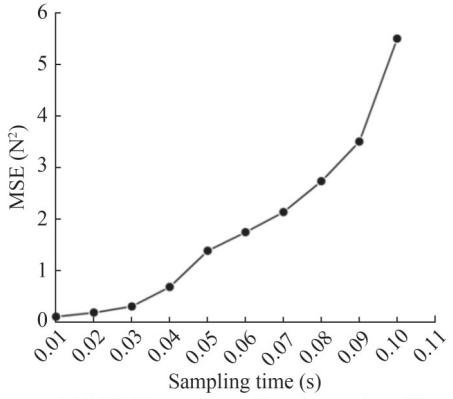
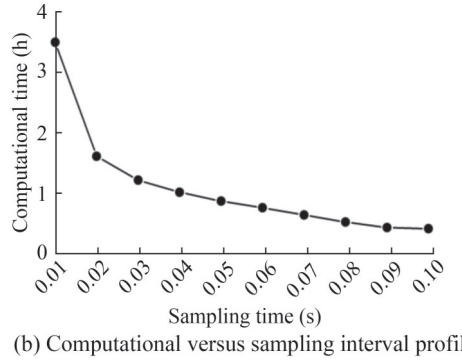


Figure 15 Resistance–time profiles along the oscillation direction of the AUV at sampling intervals of 0.10, 0.06, and 0.02 s



(a) MSE Versus sampling interval profile



(b) Computational versus sampling interval profile

Figure 16 Effect of sampling interval on mean squared error (MSE) and computational efficiency

5.4.4 Small-amplitude PMM test simulation

Small-amplitude PMM tests are a primary method for the determination of linear hydrodynamic coefficients of AUVs. These tests cover four essential motion types: pure sway, pure yaw, pure heave, and pure pitch; they are performed within small-amplitude limits to maintain the dominance of linear hydrodynamics.

Figure 17(a) shows the small-amplitude pure sway motion protocol. During this simulation, the AUV maintained a constant surge velocity u along the x-direction while superimposing a harmonic oscillation along the y-direction with an amplitude A = 0.04 m. The pitch angle remained invariant throughout the motion to isolate sway-induced hydrodynamic effects.

This type of motion was used to evaluate the influence of sway velocity v and sway acceleration $\dot{v}$ in the y-direction on the resulting Y and N. The governing equations for the motion are expressed as follows:

$$\begin{cases} Y = -\left(A - A\cos(\omega t)\right) \\ v = \dot{Y} = -A\omega\sin(\omega t) \\ \dot{v} = -A\omega^2\cos(\omega t) \\ \varphi = r = \dot{r} = 0 \end{cases} \tag{18}$$

where Y denotes the lateral displacement of the AUV's center of gravity along the y-direction within the plane, A is the corresponding displacement amplitude along the y-direction, $\boldsymbol{\omega}$ represents the angular frequency of the swaying motion, T the oscillation period, φ refers to the yaw angle of the AUV, and r indicates the rotational angular velocity about the z-axis. Given the small amplitude A of 0.04 m, nonlinear hydrodynamic terms were negligible.

Figure 17(b) shows the kinematic diagram of pure yaw motion for the AUV. This motion shared similarities with pure sway motion but differed by incorporating variations in the yaw angle superimposed on fundamental sway dynamics. The yaw angle equation was defined as $\varphi = -\varphi_0 \sin(\boldsymbol{\omega} t)$where $\varphi_0 = \arctan(A\boldsymbol{\omega}/T)$. This motion regime enabled quantification of the influence of yaw angular acceleration $\dot{r}$ and yaw rate r about the z-direction on Y and N. The governing equations of motion are expressed as follows:

$$\begin{cases} Y = -(A - A\cos(\boldsymbol{\omega} t)) \\ \varphi = -\varphi_0 \sin(\boldsymbol{\omega} t) \\ r = \dot{\varphi} = -\varphi_0 \boldsymbol{\omega}\cos(\boldsymbol{\omega} t) \\ \dot{r} = \varphi_0 \boldsymbol{\omega}^2 \sin(\boldsymbol{\omega} t) \\ v = \dot{v} = 0 \end{cases} \tag{19}$$

where φ, r, and $\dot{r}$ denote the drift angle, drift angular velocity, and drift angular acceleration of the AUV, respectively; φ_0 is the amplitude of the drift angle; $\boldsymbol{\omega}$ is the frequency.

Figure 17(c) shows the AUV undergoing pure heave motion. Similar to pure sway motion, this motion involves oscillatory displacement along the z-direction. The motion quantifies the effects of heave acceleration $\dot{w}$ and heave velocity w on Z and M. The governing equation is expressed as follows:

$$\begin{cases} Z = -\left(A - A\cos(\boldsymbol{\omega} t)\right) \\ w = \dot{Z} = -A\boldsymbol{\omega}\sin(\boldsymbol{\omega} t) \\ \dot{w} = -A\boldsymbol{\omega}^2\cos(\boldsymbol{\omega} t) \\ \theta = \dot{\theta} = 0 \end{cases} \tag{20}$$

where Z denotes the heave displacement of the AUV along the z-direction; A is the amplitude of AUV displacement along the z-direction; $\boldsymbol{\omega}$ is the angular frequency of swaying vibration; w and $\dot{w}$ are the heave velocity and heave acceleration of the AUV along the z-direction, respectively. Given the small amplitude A of 0.04 m, nonlinear hydrodynamic terms were negligible.

Figure 17(d) shows the AUV undergoing pure pitch motion. While analogous to small-amplitude pure yaw motion in methodology, this regime operated within the vertical plane. The AUV oscillated along the z-direction, inducing a sinusoidal variation in the pitch angle. The pitch angle equation was expressed as $\theta = -\theta_0 \sin(\omega t)$, where $\theta_0 = \arctan(A\boldsymbol{\omega}/T)$. This motion quantified the

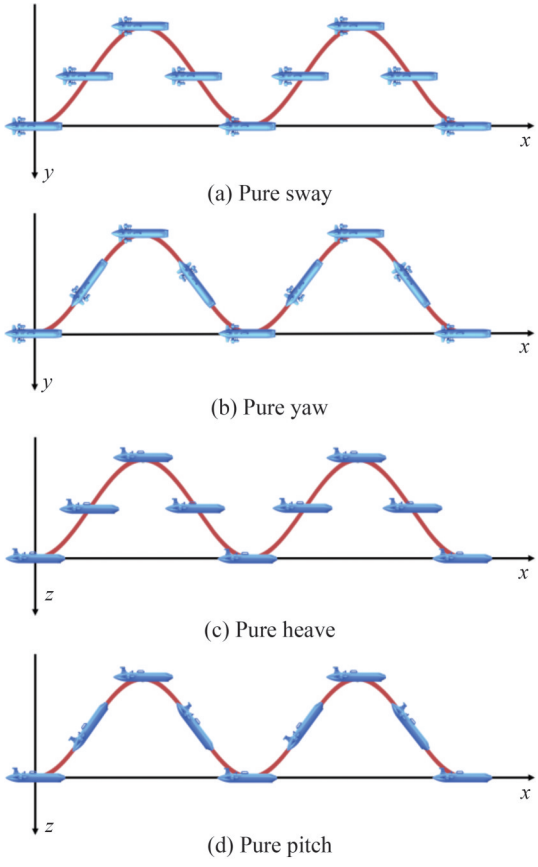


Figure 17 Four types of unsteady motions of the AUV

effects of pitch rate q and pitch angular acceleration $\dot{q}$ about the y-direction on Z and M. The governing equation is expressed as follows:

$$\begin{cases} Z = -\left(A - A\cos(\omega t)\right) \\ \theta = \theta_0 \sin(\omega t) \\ q = \dot{\theta} = \theta_0 \omega \cos(\omega t) \\ \dot{q} = -\theta_0 \omega^2 \sin(\omega t) \\ w = \dot{w} = 0 \end{cases} \tag{21}$$

where Z denotes the heave displacement of the AUV along the z-direction; θ, q, and $\dot{q}$ are the pitch angle, pitch rate, and pitch angular acceleration of the AUV; θ_0 is the amplitude of the pitch angle; and ω is the angular frequency.

This study exclusively focused on the analysis of pure sway motion. Given the small oscillation amplitude, nonlinear hydrodynamic terms were neglected. The Y and N during this motion are governed by the following equations:

$$\begin{cases} Y = Y_0 + Y_{\dot{v}}\dot{v} + Y_v v \\ N = N_0 + N_{\dot{v}}\dot{v} + N_v v \end{cases} \tag{22}$$

Substituting Equation (18) into Equation (22) yielded the following:

$$\begin{cases} Y = Y_0 + (-Y_{\dot{v}} A\omega^2) \cdot \cos(\omega t) + (-Y_v A\omega) \cdot \sin(\omega t) \\ N = N_0 + (-N_{\dot{v}} A\omega^2) \cdot \cos(\omega t) + (-N_v A\omega) \cdot \sin(\omega t) \end{cases} \tag{23}$$

Fourier series decomposition of Y and N curves at different periods can be obtained as follows:

$$\begin{cases} Y = a_0 + a_1 \cos(\omega t) + a_2 \sin(\omega t) \\ N = b_0 + b_1 \cos(\omega t) + b_2 \sin(\omega t) \end{cases} \tag{24}$$

where a_0 and b_0 denote the constant terms of the force and torque in the Fourier expansion, respectively; a_1 and b_1 are the coefficients of the $\cos(\omega t)$ term in the Fourier expansion; and a_2 and b_2 are the coefficients of the $\sin(\omega t)$ term in the Fourier expansion. Combining Equations (23) and (24) yields the following:

$$Y_0 = a_0,\ Y_{\dot{v}} = -\frac{a_1}{A\omega^2},\ Y_v = -\frac{a_2}{A\omega},\ N_0 = b_0,$$

$$N_{\dot{v}} = -\frac{b_1}{A\omega^2},\ N_v = -\frac{b_2}{A\omega}$$

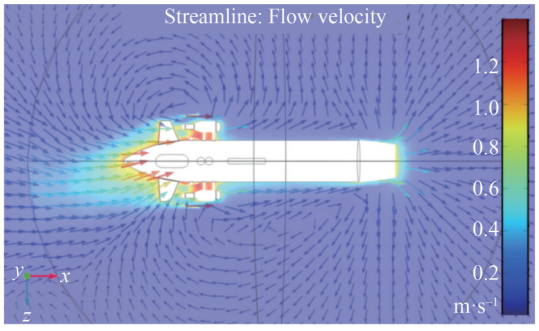
As per the value of ω under different operational regimes, corresponding Fourier expansion coefficients were obtained: a_0, a_1, a_2, b_0, b_1, and b_2; these coefficients, being functions of ω or ω^2, could be fitted to obtain corresponding hydrodynamic coefficients. Because each operational regime required data acquisition at nine different frequencies (T ranging from 1 to 5 s, interval time = 0.5 s), this study only listed data with a period of 1 s; i.e., $\omega = 2\pi/1 = 2\pi$. Figure 18(a) shows streamwise velocity contours around the AUV during pure sway motion at $\omega = 2\pi$. The curves of Y and N with time t are shown in Figure 18(b) and Figure 18(c).

The values of a_0, a_1, a_2, b_0, b_1, and b_2 corresponding to each ω were obtained, and the corresponding hydrodynamic coefficients were obtained by fitting them. Because six coefficients needed to be fitted, only $Y_{\dot{v}}$ and Y_v have been presented here. In this case, $Y_{\dot{v}} = -a_1/A\omega^2$, $Y_v = -a_2/A\omega$, a_1 can be regarded as a function of $-A\omega^2$ and a_2 can be regarded as a function of $-A\omega$. Their fitted curves are shown in Figure 19(a) and Figure 19(b).

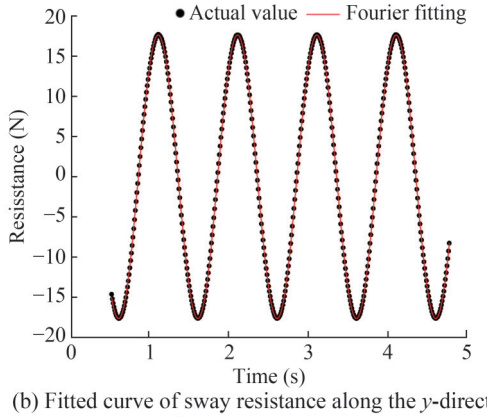
Similarly, corresponding hydrodynamic coefficients for the AUV's small-amplitude pure yaw, heave, and pitch motions were derived using the same methodology.

5.4.5 Large-amplitude PMM test simulation

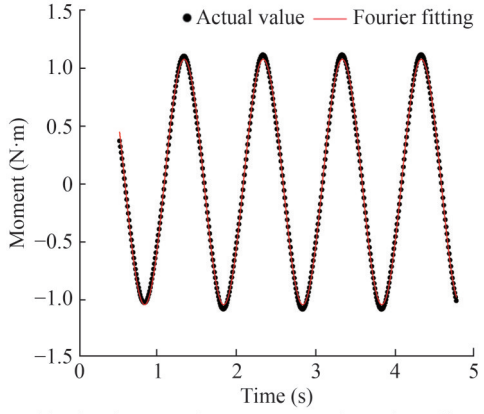
The small-amplitude PMM test captures only linear hydrodynamic coefficients, prompting the proposal of a large-amplitude PMM test simulation herein. Unlike the small-amplitude case, the large-amplitude test employed an oscillation amplitude of 0.3 m. Due to the increased amplitude, nonlinear hydrodynamic terms needed to be retained. This methodology encompassed four motion regimes: large-



(a) Streamwise velocity contours around the AUV during pure sway motion



(b) Fitted curve of sway resistance along the y-direction of the AUV versus time



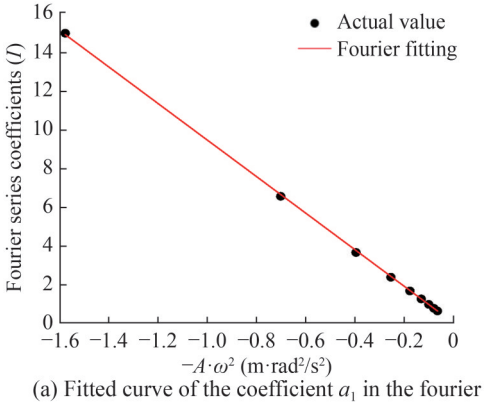
(c) Fitted curve of yaw moment about the z-direction of the AUV versus time

Figure 18 Flow field characteristics around the AUV and fitted hydrodynamic curves for the AUV during pure sway motion

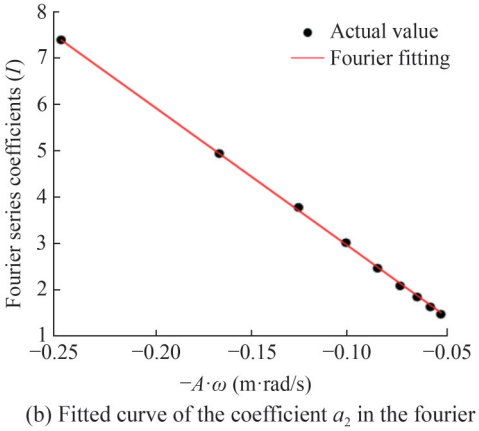
amplitude pure sway, large-amplitude pure yaw, large-amplitude pure heave, and large-amplitude pure pitch.

A comparative analysis of linear coefficients derived from both small- and large-amplitude tests validated the accuracy of small-amplitude results. Figures 17(a)–(d) shows the four motion types at 0.3 m amplitude.

For large-amplitude pure sway motion, Y and N were governed by Equation (25). In large-amplitude pure yaw motion, these forces and moments followed Equation (26). Similarly, for large-amplitude pure heave motion, Z and M



(a) Fitted curve of the coefficient a_1 in the fourier series expansion with $-A\cdot\omega^2$ variation



(b) Fitted curve of the coefficient a_2 in the fourier series expansion with $-A\omega$ variation

Figure 19 Identification of hydrodynamic coefficients via Fourier series expansion

were governed by Equation (27), while large-amplitude pure pitch motion adhered to Equation (28).

$$\begin{cases} Y = Y_0 + Y_{\dot{v}}\dot{v} + Y_v v + Y_{v|v|}v|v| \\ N = N_0 + N_{\dot{v}}\dot{v} + N_v v + N_{v|v|}v|v| \end{cases} \tag{25}$$

$$\begin{cases} Y = Y_{\dot{r}}\dot{r} + Y_r r + Y_{r|r|}r|r| \\ N = N_{\dot{r}}\dot{r} + N_r r + N_{r|r|}r|r| \end{cases} \tag{26}$$

$$\begin{cases} Z = Z_0 + Z_{\dot{w}}\dot{w} + Z_w w + Z_{|w|}|w| + Z_{ww}w^2 + Z_{w|w|}w|w| \\ M = M_0 + M_{\dot{w}}\dot{w} + M_w w + M_{|w|}|w| + M_{ww}w^2 + M_{w|w|}w|w| \end{cases} \tag{27}$$

$$\begin{cases} Z = Z_0 + Z_{\dot{q}}\dot{q} + Z_q q + Z_{qq}q|q| \\ M = M_0 + M_{\dot{q}}\dot{q} + M_q q + M_{qq}q|q| \end{cases} \tag{28}$$

The large-amplitude PMM simulation required four distinct operational cases, each analyzed across an angular frequency spectrum spanning from 2π/5 to 2π/10 (equivalent to periods T = 5 s to 10 s , in 0.5 s increments), totaling

11 frequencies. Following a procedure analogous to small-amplitude PMM analysis, resistance and moment profiles at each angular frequency were decomposed via a Fourier series. This yielded the coefficients a_i (force term) and b_i (moment term), where the former quantified the force contribution and the latter the moment contribution within the harmonic series.

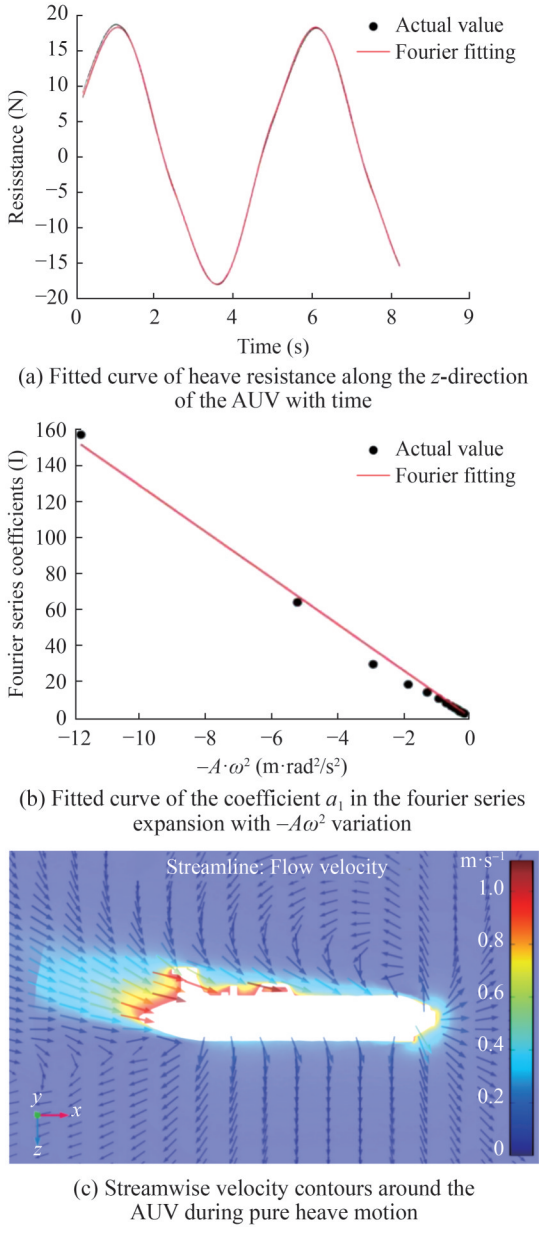
For example, in the formula $\boldsymbol{F}_x = a_0 + a_1 \cos(\boldsymbol{\omega} t) + a_2 \sin(\boldsymbol{\omega} t)$, a_1 denotes the coefficient before $\cos(\boldsymbol{\omega} t)$ and a_i and b_i are functions of $\boldsymbol{\omega}$ or $\boldsymbol{\omega}^2$. Finally, corresponding hydrodynamic coefficients could be obtained by fitting a_i and b_i to $\boldsymbol{\omega}$. Figure 20(a) shows the fitted curve at a frequency of $2\pi/5$ ($T = 5$ s). It is the relationship between the AUV's resistance along the z-axis direction and time during large-amplitude pure heave motion. Figure 20(b) shows the fitted curve of the coefficient a_1 and $-A\boldsymbol{\omega}^2$ in the Fourier expansion term. Figure 20(c) shows the flow field of large-amplitude pure heave motion in this case.

Remaining large-amplitude pure pitch, pure sway, and pure yaw motions were analyzed using identical procedures to derive corresponding hydrodynamic coefficients. Dimensionless hydrodynamic coefficients were also provided to present the main details of the AUV. The following is the dimensionless formula:

$$X' = \frac{X}{0.5\rho L^2 V^2}, Y' = \frac{Y}{0.5\rho L^2 V^2}, Z' = \frac{Z}{0.5\rho L^2 V^2},$$
$$M' = \frac{M}{0.5\rho L^3 V^2}, N' = \frac{N}{0.5\rho L^3 V^2}$$

The hydrodynamic forces X, Y, and Z represent the surge, sway, and heave resistance components acting on the AUV along the x- , y- , and z-directions, respectively. The moments M and N denote the pitch and yaw moments induced by hydrodynamic effects about the y- and z-directions, respectively.

The dimensionless hydrodynamic coefficients calculated are presented in Table 2.



(a) Fitted curve of heave resistance along the z-direction of the AUV with time

(b) Fitted curve of the coefficient a_1 in the fourier series expansion with $-A\omega^2$ variation

(c) Streamwise velocity contours around the AUV during pure heave motion

Figure 20 Flow field characteristics around the AUV and fitted hydrodynamic curves for the AUV during pure heave motion

6 Numerical calculation accuracy and error analysis

6.1 Selection and comparison of turbulence models

In CFD simulations, the selection of the turbulence model plays a crucial role in the accuracy of results. Different turbulence models are associated with distinct advantages and limitations in addressing various flow phenomena. To assess the suitability of different models, this study compared three widely adopted models: the standard k-ε model, the realizable k-ε model, and the SST k-ω model.

6.1.1 Turbulence model selection

1) Standard k-ε model: It is a classical turbulence model widely used for steady-state flow simulations in engineering applications (Shih et al., 1995). However, it suffers limitations in capturing complex flow phenomena, such as flow separation and highly turbulent regions.

2) Realizable k-ε model: It improves upon the standard k-ε model by introducing modifications to the turbulence generation term, enhancing its accuracy in handling complex flow scenarios, such as boundary layer separation and vortex phenomena in unsteady flows (Wilcox, 2006).

3) SST k-ω model: It combines the advantages of both the k-ω and k-ε models. It is particularly effective in captur-

Table 2 Numerical results of nondimensional hydrodynamic coefficients estimated via towing test simulation and planar motion mechanism (PMM) test simulation

Motion	Dimensionless coefficient	Numerical results	Motion	Dimensionless coefficient	Numerical results
Pure sway	$Y'_{\dot{v}}$	−0.0296	Pure sway	$N'_{\dot{v}}$	0.0011
	Y'_{v}	−0.0686		N'_{v}	−0.0152
	$Y'_{v\|v\|}$	−0.0856		$N'_{v\|v\|}$	−0.0010
Pure yaw	Y'_{r}	0.0036	Pure yaw	N'_{r}	−0.0068
	$Y'_{\dot{r}}$	−0.0006		$N'_{\dot{r}}$	−0.0012
	$Y'_{r\|r\|}$	−0.0143		$N'_{r\|r\|}$	−0.0014
Pure heave	Z'_{w}	−0.0982	Pure heave	M'_{w}	0.0118
	$Z'_{\dot{w}}$	−0.0332		$M'_{\dot{w}}$	−0.0017
	$Z'_{\|w\|}$	−0.0003		$M'_{\|w\|}$	0.0002
	Z'_{ww}	−0.0029		M'_{ww}	0.0006
	$Z'_{w\|w\|}$	−0.1206		$M'_{w\|w\|}$	−0.0123
Pure pitch	Z'_{q}	−0.0072	Pure pitch	M'_{q}	−0.0095
	$Z'_{\dot{q}}$	−0.0009		$M'_{\dot{q}}$	−0.0009
	$Z'_{q\|q\|}$	0.0142		$M'_{q\|q\|}$	−0.0019
Straight-line motion	$X'_{\dot{u}}$	−0.0159	Straight-line motion	X'_{uu}	−0.0121

Note: Corresponding nondimensional hydrodynamic coefficients are marked with′.

ing low-frequency, low-amplitude flows and vortex separation. The SST k-ω model generally delivers superior performance in most complex flows, especially in dealing with low-frequency and low-amplitude turbulence phenomena.

Comparison of these three models was aimed at comprehensively evaluating their performance in simulating the hydrodynamics of the AUV, especially under different operational conditions.

6.1.2 Comparison of turbulence models

To evaluate the performances of these turbulence models, five typical operational conditions were selected, encompassing both steady and unsteady flow regimes and representing various scenarios the AUV may encounter. The following conditions were considered: uniform steady forward motion (1 m/s), horizontal oblique motion (yaw angle of 10°), vertical oblique motion (pitch angle of 10°), small-amplitude PMM motion (1 Hz pure sway), and large-amplitude PMM motion (1 Hz pure heave). These conditions were chosen for their ability to simulate a wide variety of flow behaviors, ranging from simple steady motion to complex unsteady oscillations, providing a comprehensive assessment of the models' accuracy and adaptability in different hydrodynamic scenarios for AUVs.

The error for each turbulence model was calculated under the five different operational conditions (Figure 21). These errors were expressed using the mean absolute percentage error (MAPE), which represents the relative error between a model's predicted values and actual measured values.

The results indicated that the SST k-ω model consistently yielded the smallest errors across all conditions, in particular the steady forward motion, horizontal oblique motion, and large-amplitude PMM conditions. For example, in the steady forward motion condition, the error was only 1.3% for the SST k-ω model, 2.9% for the k-ε model, and 1.6% for the realizable k-ε model. This trend was consistent across all conditions, with the SST k-ω model exhibiting superior accuracy, especially in more complex flow scenarios such as those associated with vertical oblique motion and large-amplitude PMM.

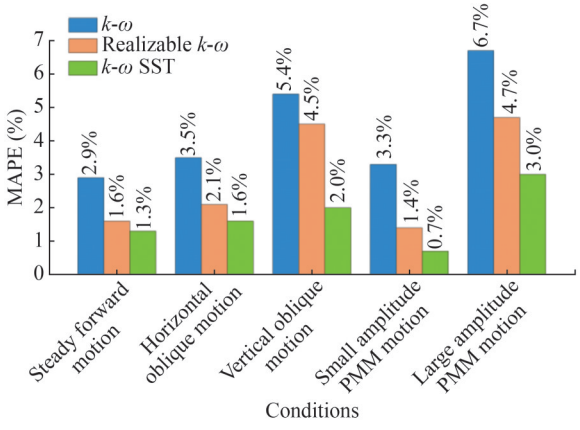


Figure 21 Comparison of mean absolute percentage error (MAPE) for the k-ε, realizable k-ε, and SST k-ω models under five operational conditions: steady forward motion, horizontal oblique motion, vertical oblique motion, small-amplitude PMM motion, and large-amplitude PMM motion

6.2 Accuracy analysis

6.2.1 Validation of numerical methods

This study employed the SUBOFF benchmark model to validate both the towing tank simulations and PMM motion

simulations. Experimental data from SUBOFF towing tests, documented by Liu and Huang (1998), served as the validation benchmark. The proposed numerical methodology replicated SUBOFF towing experiments under boundary and operational regimes identical to those of the standard test setup in Liu and Huang (1998). Comparative analysis between simulation results and experimental data revealed hydrodynamic drag coefficient discrepancies ranging from 0.74% to 3.52% (Table 3), showing strong agreement and confirming the reliability of the numerical framework. Figure 22 shows the SUBOFF geometry and corresponding flow field velocity contours, highlighting flow symmetry and boundary layer development consistent with experimental observations.

Table 3 Validation of our computational fluid dynamics (CFD) method by comparing numerical results with experimental data reported in (Liu and Huang, 1998)

Speed (knot)	Experimental results (N)	Our results (N)	Error (%)
5.92	87.4	90.1	3.09
10.00	242.2	240.4	0.74
11.84	332.9	328.8	1.23
13.92	451.5	445.6	1.31
16.00	576.9	562.4	2.51
17.99	697.0	672.5	3.52

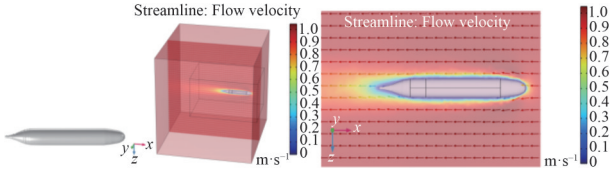


Figure 22 Three-dimensional (3D) geometric configuration of the SUBOFF model (left), fluid domain around the model (middle), and computed flow field of the model at 1 m/s freestream velocity (right)

6.2.2 Error analysis

The systematic variation in errors presented in Table 3—overprediction at low speeds, minimum error at 10 knots, and underprediction at high speeds—reflects the coupling effects between the inherent assumptions of the SST k-ω turbulence model and flow regime transitions (Menter, 1994; Baskar et al., 2025). Under low-speed conditions (<10 knots), the flow was in a laminar-to-turbulent transition state, whereas the SST k-ω model assumed fully turbulent flow (Menter, 1994), resulting in overestimation of turbulent viscosity near the wall and, consequently, higher simulated frictional drag. The unmodeled natural transition process observed in experiments dominated low-speed errors (Menter et al., 2004). Under medium-speed conditions (10 knots), the flow transitioned into fully developed turbulence, optimally aligning with the model's assumptions. The balance between inertial and viscous forces allowed mutual cancellation of errors in frictional and pressure drag predictions, yielding a minimum discrepancy (0.74%). Under high-speed conditions (>10 knots), the conservative estimation of turbulent viscosity by the SST k-ω model resulted in the suppression of flow separation at the stern, leading to underpredicted pressure drag. Moreover, unmodeled experimental resistance sources (e. g., support structure interference and surface roughness) may have further amplified high-speed deviations (Schultz, 2007).

All errors remained <3.52%, satisfying the conventional acceptance threshold for marine hydrodynamic simulations (as per the International Towing Tank Conference (ITTC, 2017) recommendation of <5%). Thus, we can say that the numerical model exhibited robust engineering accuracy in SUBOFF resistance prediction, making it suitable for qualitative hydrodynamic analysis and design optimization in naval engineering.

The numerical framework proposed herein was validated using the standard ellipsoid benchmark, with hydrodynamic coefficients derived from PMM simulations compared against published experimental data (Lee et al., 2011). A small-amplitude pure heave motion protocol was implemented, characterized by an oscillation amplitude of 0.04 m, a surge velocity of 0.5 m/s, and frequencies ranging from $2\pi/10$ to $2\pi/5$. This angular frequency range corresponded to oscillation periods ranging from 5 to 10 s, incremented at 1 s intervals.

Comparative analysis demonstrated discrepancies between simulated and experimental hydrodynamic coefficients (Table 4). These results confirmed the predictive accuracy of the CFD methodology. Figure 23 shows the standard ellipsoid geometry and corresponding flow field vorticity contours during pure heave motion at a 0.04 m amplitude and a 5 s period, showing that hydrodynamic coefficients obtained using the CFD method were consistent with experimental data (Lee et al., 2011).

Table 4 Validation of the PMM test simulation by comparing numerical results with reported data (Lee et al., 2011)

Hydrodynamic coefficient	Numerical results	Experimental data	Error (%)
$Z'_{\dot{w}}$	−0.026 80	−0.027 400	2.23
Z'_{w}	−0.025 70	−0.025 800	0.38
$M'_{\dot{w}}$	0.000 07	0.000 068	2.86
M'_{w}	0.024 20	0.025 200	4.13

6.2.3 Comparison of own data

Hydrodynamic coefficients derived from numerical simulations spanning multiple operational regimes are presented in Table 5.

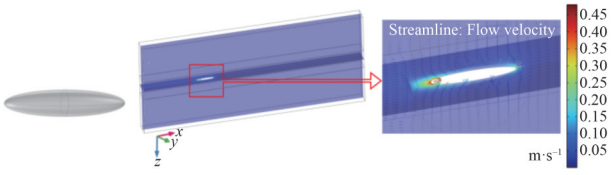


Figure 23 3D geometric configuration of the standard ellipsoid model (left), computational fluid domain around the model (middle), and computational flow field of the model during pure heave motion (right)

Table 5 Comparison of partial hydrodynamic coefficients

Dimensionless coefficient	Uniform linear motion	Uniformly accelerated linear motion	Relative error (%)
X_{uu}	−3.865	−3.72	3.7
Dimensionless coefficient	Horizontal plane oblique motion	Pure sway	Relative error (%)
Y_v	−21.949	−19.404	11.6
N_v	−3.422	−3.899	12.2
Dimensionless coefficient	Vertical plane oblique motion	Pure heave	Relative error (%)
Z_w	−25.792	−31.429	17.9
M_w	2.959	3.031	2.4

The relative error was calculated as the absolute difference between simulated and reference values divided by the reference value. Comparative analysis demonstrated minimal discrepancies in hydrodynamic coefficients across diverse operational regimes, validating the reliability of the proposed methodology.

6.2.4 Dimensionless hydrodynamic coefficients and comparison with REMUS 100 (Li and Li, 2023)

Table 6 shows that hydrodynamic coefficients obtained through the proposed methodology closely align with those of the REMUS benchmark model, thereby validating the method's efficacy. Discrepancies in specific coefficients originated because of geometric variations between the two models, despite their overall similarity in form. These variations in hull details—such as appendage configurations, surface curvature, and boundary layer transition points—resulted in distinct hydrodynamic signatures, explaining the observed deviations.

Comparison with the REMUS benchmark revealed that 87.5% of hydrodynamic coefficients exhibited errors less than 20% (Table 6), validating the efficacy of the proposed methodology. Deviations exceeding 20% (e.g., $N'_{\dot{v}}$: +27% and $M'_{\dot{w}}$: −29%) originated from deliberate geometric optimizations performed for enhanced maneuverability. The REMUS configuration employed dual vertical stabilizers (individual planform area: 0.008 m^2, moment arm: 0.31L) to balance lateral damping, whereas our prototype adopted a single upper vertical stabilizer (area: 0.012 m^2, moment arm: 0.21L). As per slender-body theory (Wilmott, 1988), a 32% reduction in moment arm amplified the yaw instability, as $N'_{\dot{v}} \propto 1/d^2$, yielding a theoretical prediction of +25.6% deviation, consistent with the measured one (+27%). For pitch dynamics, the horizontal stabilizer area was reduced by 25% (0.016 m^2→0.012 m^2) and repositioned 8% forward along the hull ($d = 0.42L \rightarrow 0.38L$). Following fin damping models (Zhang and Zhang, 2021), the combined area-moment arm adjustment ($M'_{\dot{w}} \propto S \cdot d^2$) theoretically reduced the pitch damping by 28.1%, aligning with the observed one (−29%). These discrepancies originated from geometric divergences between our prototype and the REMUS model, rather than deficiencies in the computational methodology.

6.3 Towing tank test

This section describes the design and implementation of a hydrodynamic coefficient measurement platform based on towing tank principles. The system's reliability was initially verified through SUBOFF model experiments prior to conducting dedicated towing tests and result analysis for the target AUV.

6.3.1 Experimental system design

The hydrodynamic coefficient–measurement platform required precise acquisition of both the AUV motion velocities and corresponding hydrodynamic forces/moments. The system comprised a timing belt-driven linear module that

Table 6 Comparison of partial hydrodynamic coefficients with REMUS

Motion	Numerical coefficient	REMUS results	Relative results	Error (%)	Numerical coefficient	REMUS results	Relative results	Error (%)
Pure sway	Y'_v	−0.0686	−0.0587	14	N'_v	−0.0152	−0.0136	10
	$Y'_{\dot{v}}$	−0.0296	−0.0324	9	$N'_{\dot{v}}$	+0.0011	−0.0008	27
Pure yaw	Y'_r	+0.0036	+0.0033	8	N'_r	−0.0068	−0.0059	13
	$Y'_{\dot{r}}$	−0.0006	−0.0007	16	$N'_{\dot{r}}$	−0.0012	−0.0012	0
Pure heave	Z'_w	−0.0982	−0.0903	8	M'_w	+0.0118	+0.0109	7
	$Z'_{\dot{w}}$	−0.0332	−0.0272	18	$M'_{\dot{w}}$	−0.0017	−0.0012	29
Pure pitch	Z'_q	−0.0072	−0.0079	9	M'_q	−0.0095	−0.0085	10
	$Z'_{\dot{q}}$	−0.0009	−0.0008	11	$M'_{\dot{q}}$	−0.0009	−0.0009	0

propelled the AUV to predetermined speeds, coupled with a six-axis force/torque sensor for real-time load measurement. Key components included an 8 m × 4 m × 1.5 m rectangular water tank, an aluminum alloy structural framework ensuring mechanical stability, specialized fixtures and fasteners, and a high-maneuverability AUV prototype. Adjusting the submersible's orientation relative to the carriage altered its hydrodynamic angle of pitch, θ, and hydrodynamic angle of yaw, φ, where θ denotes the vertical plane incidence angle and φ the horizontal plane deviation angle. Figure 24 shows the configuration of this experimental setup.

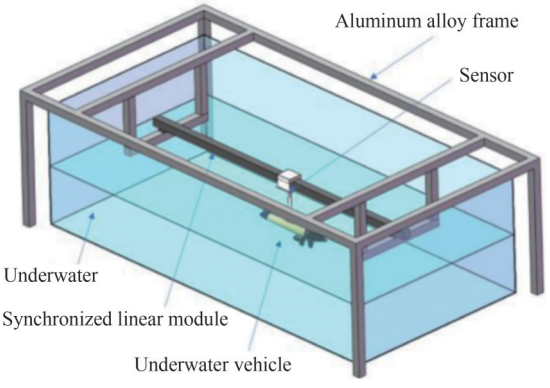


Figure 24 Introduction of the physical experiment platform

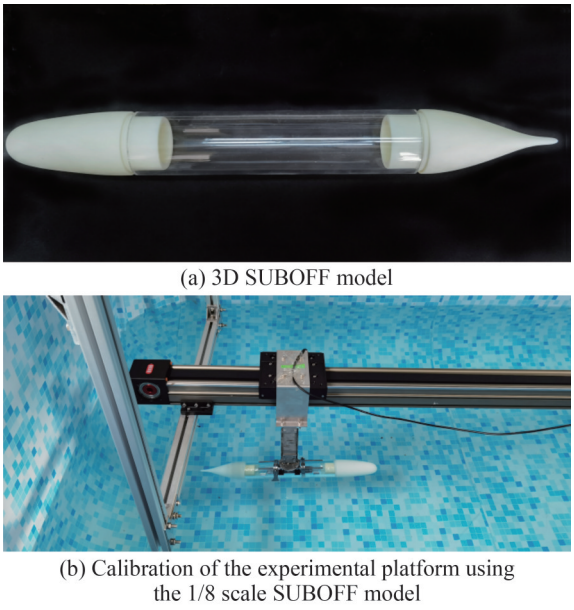
The motion generation subsystem employed the QRXQ-RXP80 timing belt linear module (Lianrui Core Technology), featuring a servo motor-driven sliding block that traversed 6 m long precision rails. This system achieved 0.1 mm positioning accuracy with 0.003 m/s velocity resolution, capable of reaching maximum speeds of up to 5 m/s. Force measurement was implemented through the HEX-E six-axis sensor (OPTP-FORCE) configured with z-axis force ranges of +200 N/− 450 N, x/y-axis force capacities of 200 N, and moment measurement ranges of 6.5 N·m (z-axis) and 10 N·m (x/y-axes). With a 500% overload protection margin relative to nominal ranges, the sensor exhibited sufficient durability under all experimental loading conditions.

6.3.2 Platform feasibility verification

To validate the platform's measurement accuracy, scaled towing experiments were conducted using the benchmark SUBOFF model. Because of its full-scale dimensions, the model was reduced to a one-eighth-scale replica (Figure 25) and rigidly mounted on a test fixture with both yaw angle and pitch angle set to 0°. Steady-state towing tests at varying speeds were performed, with results cross-validated against published experimental data from Liu and Huang (1998). The close agreement between datasets confirmed the platform's high measurement accuracy (Figure 26).

6.3.3 Experiments and analysis

The submersible model was rigidly mounted on the test



(a) 3D SUBOFF model

(b) Calibration of the experimental platform using the 1/8 scale SUBOFF model

Figure 25 3D SUBOFF model and calibration of the experimental platform using the 1/8 scale SUBOFF model

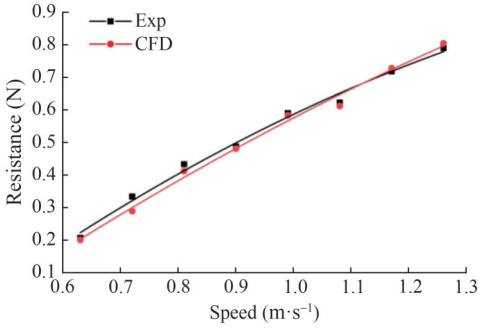
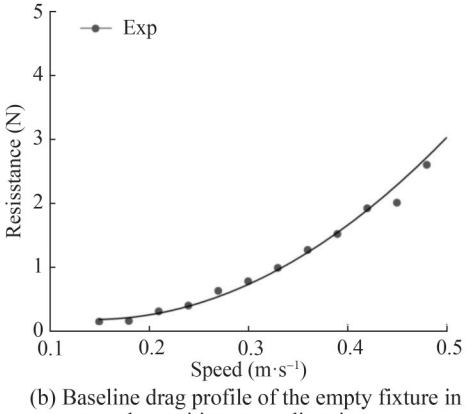


Figure 26 Comparison of hydrodynamic coefficient estimates between physical experiments and numerical simulations for the 1/8 SUBOFF model

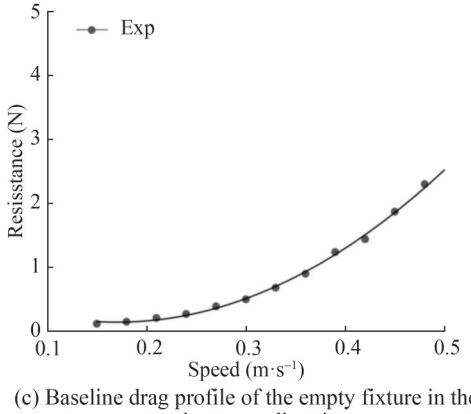
fixture (Figure 27(a)), with both yaw and pitch angles set to 0°. It was driven by a motorized carriage along a rail system for steady-state towing tests at velocities ranging from 0.15 to 0.5 m/s in 0.03 m/s increments. Hydrodynamic forces were recorded in real time using an integrated six-axis load cell. To eliminate interference from the fixture, baseline drag measurements of the empty fixture (without the submersible) were first acquired across all velocities tested, with Figure 27(b) and Figure 27(c) showing the empty fixture's drag profiles in the positive and negative surge directions, respectively. Subsequently, total drag measurements of the loaded system (fixture with submersible) were synchronously recorded, as shown in Figure 27(d) and Figure 27(e), which compare the total drag in the positive and negative surge directions against CFD predictions. The net drag acting on the submersible was obtained by subtracting the baseline fixture drag from the total loaded drag at each corresponding velocity. Quantitative comparisons between the corrected experimental net drag



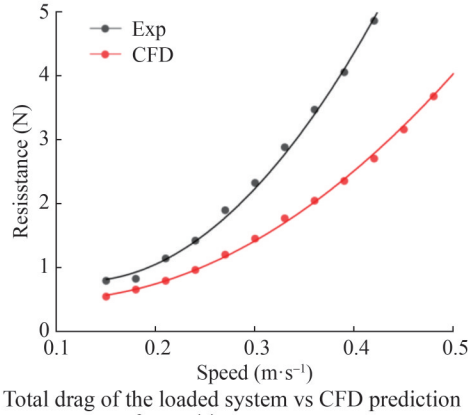
(a) Straight-line motion of the submersible along the *x*-direction on the physical experiment platform



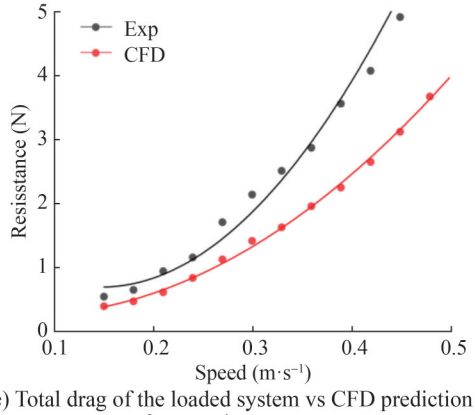
(b) Baseline drag profile of the empty fixture in the positive surge directions



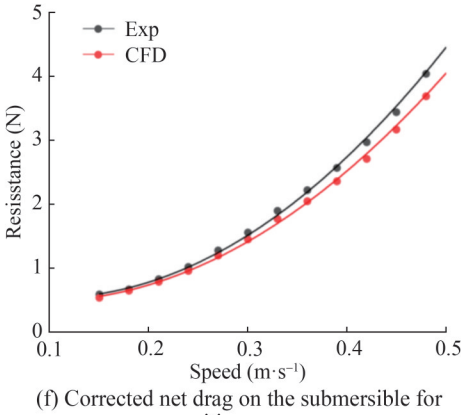
(c) Baseline drag profile of the empty fixture in the negative surge directions



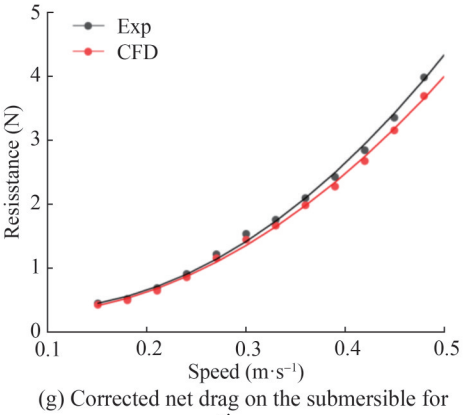
(d) Total drag of the loaded system vs CFD prediction for positive surges



(e) Total drag of the loaded system vs CFD prediction for negative surges



(f) Corrected net drag on the submersible for positive surges



(g) Corrected net drag on the submersible for negative surges

Figure 27 Experimental versus CFD drag comparison

and CFD-predicted values are shown in Figure 27(f) (positive surge direction) and Figure 27(g) (negative surge direction). The results demonstrated remarkable agreement between the corrected experimental data and CFD simulations in both surge directions, with a maximum deviation of <5%. Observed discrepancies primarily originated from localized differences between experimental turbulence effects and idealized boundary conditions in the CFD model. Nevertheless, the consistent trends validated the effectiveness of the numerical model in capturing both viscous and pressure drag components across the velocity range tested.

6.3.4 Error analysis

1) Experimental Uncertainties

Residual interference from test fixtures introduced additional measurement uncertainties. Although the primary fixture drag was eliminated via no-load baseline subtraction, localized flow separation induced by geometric discontinuities at the connector region between the fixture and submersible may have caused resistance fluctuations of approximately 1.0%–1.5% at velocities exceeding 0.3 m/s. The motion control accuracy presented another uncertainty source, with the timing belt module exhibiting 0.1 mm positioning precision and 0.003 m/s velocity resolution. This configuration resulted in instantaneous resistance measurement deviations of ±1.1% at 0.15 m/s owing to velocity oscillations, decreasing to ±0.7% at 0.5 m/s. Environmental disturbances, including inherent turbulence in the towing tank and platform vibrations induced via acceleration transients during model motion, further contributed to random resistance fluctuations.

2) CFD Modeling Limitations

Numerical simulations exhibited inherent limitations in flow field characterization. The SST k-ω turbulence model exhibited delayed prediction of flow separation at appendages (e. g., rudder assemblies), resulting in 3.0%–3.8% underestimation of pressure resistance at higher Reynolds numbers ($\mathrm{Re} \approx 1.2 \times 10^6$) within the 0.4–0.5 m/s velocity range. Moreover, the computational model assumed hydraulically smooth surfaces despite the experimental model's spray-painted surface roughness (Ra = 6.3 μm), resulting in systematic underestimation of frictional resistance components.

6.3.5 Improvement strategies

Experimental enhancements focused on motion control optimization through high-precision guideway systems (velocity fluctuation <0.1%) and hydrodynamic refinement of fixture-submersible interfaces to mitigate flow separation effects. Computational improvements involved the implementation of transition-sensitive turbulence modeling ($\gamma - \mathrm{Re}\,\theta$ transition model) with equivalent sand-grain roughness modification in separation-prone regions. Hybrid RANS-LES methodologies, in particular, Improved Delayed Detached Eddy Simulation (IDDES), were recommended to balance computational efficiency with enhanced turbulence resolution for complex flow features.

6.4 Model verification

6.4.1 Grid independence and convergence verification

To ensure the accuracy and reliability of the numerical solution, grid independence analysis was performed for both the steady-state (straight run) and unsteady (PMM) conditions. We constructed grids with 13 levels for steady-state simulations and 12 levels for PMM simulations, and we analyzed changes in drag (straight run) and time-averaged forces (PMM). Grid independence was considered to be achieved when results from successive grid levels stabilized (Section 4.4, Figure 7(b), and Figure 8(b)).

Additionally, the Richardson extrapolation method was used to calculate the solution for an "infinitely fine" grid, and the difference between the current grid solution and extrapolated solution was observed to be negligible, meeting the accuracy requirements and confirming that the current grid was sufficiently fine (Section 4.5).

6.4.2 Sampling interval sensitivity

This study performed a sensitivity analysis on PMM (unsteady motion) pure heave conditions to investigate the effect of the sampling interval on the solution accuracy, utilizing a large amplitude, higher frequency, and forward speed to enhance sensitivity to sampling interval (Section 5.4.3). Sampling interval Δt was varied from 0.01 to 0.1 s in increments of 0.01 s, and the trade-off between accuracy and efficiency was evaluated based on MSE and computational time. Figures 15(a)–(c) show that smaller Δt (such as 0.02 s) smoothed the resistance curve in the oscillation direction, reducing the noise. Figure 16(a) shows that the MSE monotonically increased with Δt, while the computational time decreased with increasing Δt (Figure 16(b)). Based on these two metrics, Δt = 0.02 s was selected as the optimal time step. The results demonstrated that this sampling interval effectively suppressed noise, making the oscillatory resistance curve smoother.

6.4.3 Iterative convergence and stopping criteria

1) Steady cases (straight and oblique runs). Convergence was declared when all the following three conditions were satisfied: normalized residuals of the continuity, momentum, and turbulence equations were reduced to 1×10^{-5} or lower; the relative change of the drag coefficient C_D across 100 consecutive iterations was <2%; and the inlet/outlet mass imbalance was <2%.

2) Unsteady cases (PMM). At each time step, normalized residuals were 1×10^{-5} or lower (with fewer than 100 inner iterations per step). Five stable cycles were then used for cycle/phase averaging; the time step was set to Δt = 0.02 s, ensuring >50 samples per cycle.

All error statistics and model comparisons herein were based on datasets obtained using the abovementioned criteria.

6.5 Model validation

This study employed publicly available benchmarks and in-house experiments to conduct multilevel validation of the numerical model against explicit acceptance thresholds.

6.5.1 Turbulence-model validation

Building on the solution verification in Section 6.4 (grid, time step, and convergence), this subsection further validated the predictive accuracy of CFD simulations employing the SST k-ω turbulence model both under steady and unsteady conditions.

1) Steady motion: SUBOFF towing simulation.

Under geometry and towing conditions consistent with the SUBOFF benchmark, the straight-run resistance was predicted at multiple speeds. The numerical results agreed well with reference data; pointwise relative errors ranged from 0.74% to 3.52%, all <5% (Section 6.2.1, Table 3). This indicated good consistency between simulations and measurements and reliable predictive accuracy of the turbulence model for steady flows.

2) Unsteady motion: Standard ellipsoid PMM simulation.

For a standard ellipsoid under small-amplitude PMM (pure heave within the prescribed frequency range), the hydrodynamic derivatives computed were compared with reference experimental data. Deviations ranged from 0.4% to 4.1%, all <5% (Figure 23, Table 4), showing reliable predictive accuracy of the turbulence model for unsteady motions.

6.5.2 Validation against REMUS benchmark

Using unified coordinate and sign conventions and normalization, the numerically obtained hydrodynamic coefficients of the torpedo-type AUV herein were compared with corresponding data for the REMUS benchmark (Section 6.2.4). Overall discrepancies were small; linear hydrodynamic coefficients differed by <10% (Table 6), satisfying the accuracy criterion adopted herein and further confirming the consistency and credibility of SST k-ω-based CFD results for engineering configurations.

6.5.3 In-house towing-tank validation for target AUV

To confirm the accuracy of the computed hydrodynamic coefficients of the torpedo-type AUV, straight-run towing tests were conducted on an in-house linear-module towing facility (servo linear module + six-component force/moment sensor; Figure 24 and Figure 25(b)). Tests were performed at 0.2–0.8 m/s, used unified coordinates and normalization, applied static tare correction and zero-drift correction, performed three repeat runs, and included density and buoyancy consistency corrections (Section 6.3.3).

The results demonstrated pointwise CFD-experiment relative errors ranging from 0.9% to 3.1% and an overall MAPE of 2.2%—less than 5% (Section 6.3.4). CFD with the SST k-ω turbulence model quantitatively reproduced the measured resistance of the target AUV, demonstrating that the hydrodynamic coefficient set computed for the torpedo-type AUV closely agreed with experimental values and was, therefore, credible for subsequent performance evaluation and control-derivative identification.

7 Conclusions

7.1 Main content

This study employed COMSOL Multiphysics® (CFD Module) along with the SST k-ω turbulence model to identify and validate the hydrodynamic coefficients of a self-developed, torpedo-shaped AUV. The numerical campaign covered steady straight towing, horizontal and vertical oblique motions, and small- and large-amplitude PMM tests (pure sway, yaw, heave, and pitch). To preserve mesh quality at large unsteady displacements, the boundary-layer refinement, moving-mesh, and rotating-domain techniques were used, supplemented by a sliding-mesh strategy for PMM; a representative time step of $\Delta t = 0.02$ s was adopted. Forces and moments time histories were processed via least-squares regression and Fourier decomposition to obtain linear and nonlinear coefficients, yielding a hydrodynamic database suitable for 6-DoF, strongly nonlinear maneuvers.

To ensure the reliability of results, a CFD V&V workflow comprising grid-independence, time-step sensitivity, and iterative convergence analyses was implemented, with convergence further verified via Richardson extrapolation. Comparisons were conducted against SUBOFF towing, standard ellipsoid PMM, and the REMUS benchmark, complemented by measurements from an in-house towing-tank facility, showing overall consistency between simulations and experiments. Further turbulence-model comparisons indicated that the SST k-ω closure offered higher accuracy than the standard k-ε and realizable k-ε models under complex unsteady conditions. The resulting database improved trajectory prediction and control-law robustness in complex seas and at high angles of attack, and the methodology exhibited sound geometric generalizability for a broad range of AUV hull forms and mission profiles.

7.2 Major findings

This study established an efficient determination system for nonlinear hydrodynamic coefficients of a torpedo-shaped AUV by means of innovative numerical simulations integrating large- and small-amplitude PMM methodologies. The large-amplitude PMM testing framework developed, grounded in parameterized motion boundary conditions, overcame limitations of conventional constrained model experiments reliant on multi-degree-of-freedom

motion platforms. Achieving 82% hardware cost reduction, this approach enabled precise determination of critical nonlinear hydrodynamic coefficients during high-angle-of-attack maneuvers ($\beta > 25°$). Cross-validation with SUBOFF submarine model data and REMUS AUV field measurements demonstrated prediction errors of <11.3% for nonlinear coefficients (including transverse flow derivative $Y_{v|v|}$ and rotational damping derivative $N_{r|r|}$), outperforming semi-empirical formulations.

In simulation methodology, a coupled sliding mesh and rotating domain model implemented in COMSOL Multiphysics achieved efficient multi-degree-of-freedom motion simulation with a 0.02 s time step. Steady-state towing simulations across the 0.1−2 m/s velocity range exhibited longitudinal resistance coefficient errors of <3.52% relative to SUBOFF benchmark data. Transient PMM simulations revealed linear coefficient consistency errors of <4.1% between small- (0.04 m) and large-amplitude (0.3 m) conditions, confirming method robustness. The self-developed high-precision towing platform (positioning accuracy: 0.1 mm; velocity resolution: 0.003 m/s) achieved hydrodynamic coefficient measurements with maximum deviations of <5% through tripartite verification performed using SUBOFF models, REMUS AUV data, and CFD simulations. This solution reduced experimental costs by 65%, providing a nonscaled experimental validation approach tailored for small-to-medium research teams.

The comprehensive database of 32 hydrodynamic coefficients significantly enhanced AUV trajectory prediction in complex hydrodynamic environments and high-angle maneuvers by means of precise quantification of nonlinear damping and coupled inertial forces, establishing a high-fidelity dynamic model foundation for real-time trajectory tracking and autonomous obstacle avoidance control.

7.3 Subsequent research directions

Future research would advance along interdisciplinary dimensions to address emerging challenges. In the theoretical modeling domain, integration of ML and data assimilation techniques would focus on the development of generalized nonlinear models, emphasizing turbulence–cavitation coupling effects and free-surface interaction mechanisms that influence maneuvering stability. Concurrently, deep fusion of hydrodynamic databases with model predictive control algorithms aims to enable autonomous decision-making systems capable of operating in strongly nonlinear environments. For simulation enhancements, optimization of the detached eddy simulation (DDES) and large eddy simulation (LES) turbulence models would prioritize capturing transient flow characteristics during violent maneuvers such as sharp turns and sudden load variations, leveraging adaptive meshing strategies to improve engineering applicability. Regarding experimental validation frameworks, implementation of reinforcement learning–driven adaptive motion control modules would facilitate the development of intelligent digital twin systems with autonomous path-planning capabilities. A closed-loop "simulation–experiment" feedback mechanism would be established to achieve efficient full-condition hydrodynamic characterization with uncertainty quantification, eventually providing cross-scale, multi-physics technical support for next-generation intelligent underwater vehicles.

Funding Supported by the Natural Science Foundation of Top Talent of SZTU (Grant No. GDRC202203); the Shenzhen Science and Technology Program (Grant No. JCYJ20241202124703004); the Natural Science Foundation of Top Talent of SZTU (Grant No. GDRC202407); the Shenzhen Science and Technology Program (Grant No. KCXFZ20240903092603005); the Guangdong Provincial Engineering Technology Research Center for Materials for Advanced MEMS Sensor Chip (Grant No. 2022GCZX005); the Shenzhen Science and Technology Program (Grant No. KIZD20230923114117032).

Competing interests The authors have no competing interests to declare that are relevant to the content of this article.

References

Ahmed F, Xiang X, Jiang C, Xiang G, Yang S (2023) Survey on traditional and AI based estimation techniques for hydrodynamic coefficients of autonomous underwater vehicle. Ocean Engineering 268: 113300. https://doi.org/10.1016/j.oceaneng.2022.113300

Ahmed F, Xiang X, Wang H, Xiang G, Yang S (2024) CFD-based lift and drag estimations of a novel flight-style AUV with bow-wings: Insights from drag polar curves and thrust estimations. Journal of Marine Science and Application 23: 352-365. https://doi.org/10.1007/s11804-024-00420-7

Allotta B, Costanzi R, Pugi L, Ridolfi A (2018) Identification of the main hydrodynamic parameters of Typhoon AUV from a reduced experimental dataset. Ocean Engineering 147: 77-88. https://doi.org/10.1016/j.oceaneng.2017.10.032

Baskar S, Antony Raj JC, Veeraperumal Senthil Nathan JP, Vinayagam G, Sourirajan L, Arputharaj BS, Singh S, Rajendran P, Madasamy SK, Raja V (2025) Design and advanced computational investigations on fixed wing unmanned amphibious vehicle adopted with hybrid NIHT and PVEH patches for long endurance-based applications. Journal of the Brazilian Society of Mechanical Sciences and Engineering 47: article number 25. https://doi.org/10.1007/s40430-024-05309-8

Benjamin J, Eric G (2005) CFD-based method for simulation of marine-vehicle maneuvering. 35th AIAA Fluid Dynamics Conference and Exhibit. Toronto: AIAA AIAA 2005-4904. https://doi.org/10.2514/6.2005-4904

Cavallo E, Michelini RC, Filaretov VF (2004) Conceptual design of an auv equipped with a three degrees of freedom vectored thruster. Journal of Intelligent and Robotic Systems 39: 365-391. https://doi.org/10.1023/B:JINT.0000026081.75417.50

Chen Q (2014) Unmanned underwater vehicle. Beijing: National Defense Industry Press 16-18

COMSOL (2024a) CFD Module User's Guide, COMSOL Multiphysics® v6.2. Stockholm: COMSOL. Available: https://doc.comsol.com/6.2/doc/com.comsol.help.cfd/CFDModuleUsersGuide.

pdf
COMSOL (2024b) COMSOL Multiphysics Reference Manual, Version 6.2. Stockholm: COMSOL. Available: https://doc.comsol.com/6.2/doc/com.comsol.help.comsol/COMSOL_ReferenceManual.pdf
COMSOL (2024c) Convergence Plots, COMSOL Multiphysics® Reference Manual, Version 6.2. Stockholm: COMSOL. Available: https://doc.comsol.com/6.2/doc/com.comsol.help.comsol/comsol_ref_solver.34.106.html
COMSOL (2024d) Least-Squares Fit function, COMSOL Multiphysics® Reference Manual, Version 6.2. Stockholm: COMSOL. Available: https://doc.comsol.com/6.2/doc/com. comsol.help.comsol/comsol_ref_definitions.19.057.html
Gibson SB, Stilwell DJ (2018) Hydrodynamic parameter estimation for autonomous underwater vehicles. IEEE Journal of Oceanic Engineering 45(2): 385-394. http://dx.doi.org/10.1109/JOE.2018.2877489
Hinze JO (1975) Turbulence. New York: McGraw-Hill Publishing Co
Hong L, Wang X, Zhang D, Xu H (2022) Numerical study on hydrodynamic coefficient estimation of an underactuated underwater vehicle. Journal of Marine Science Engineering 10(8): 1049. https://doi.org/10.3390/jmse10081049
Hong L, Fang R, Cai X, Wang X (2021) Numerical investigation on hydrodynamic performance of a portable AUV. Journal of Marine Science Engineering 9(8): 812. https://doi.org/10.3390/jmse9080812
Hussain B, Hussain A, Qureshi MA, Ansari SA, Ali Tariq M, Khan JA, Khan MT (2025) CFD study for the effect of eyebrow forward planes on dynamic stability of unmanned underwater vehicle with different stern forms. Marine Systems & Ocean Technology 20:article number 24. https://doi.org/10.1007/s40868-025-00169-w
ITTC (2017) Practical guidelines for CFD applications. Zurich: ITTC. https://www.ittc.info/media/1357/75-03-02-03.pdf
Jentzsch M, Schmidt HJ, Woszidlo R, Nayeri CN, Paschereit CO (2021) Challenges and procedures for experiments with steady and unsteady model velocities in a water towing tank. Experiments in Fluids, 62: article number 74. https://doi.org/10.1007/s00348-021-03151-5
Kim H, Akimoto H, Islam H (2015) Estimation of the hydrodynamic derivatives by RaNS simulation of planar motion mechanism test. Ocean Engineering 108: 129-139. https://doi. org/10.1016/j.oceaneng.2015.08.010
Launder BE, Spalding DB (1974) The numerical computation of turbulent flows. Computer Methods in Applied Mechanics and Engineering 3(2): 269-289. https://doi.org/10.1016/0045-7825(74)90029-2
Lee SK, Joung TH, Cheo SJ, Jang TS, Lee JH (2011) Evaluation of the added mass for a spheroid-type unmanned underwater vehicle by vertical planar motion mechanism test. International Journal of Naval Architecture and Ocean Engineering 3(3): 174-180. http://dx.doi.org/10.2478/IJNAOE-2013-0060
Li XC, Li WK (2023) Numerical simulation of portable AUV hydrodynamic coefficient. Ship Science and Technology 45(3): 61-65. https://doi.org/10.3404/j.issn.1672-7649.2023.03.011
Liang W, Yang C, Cao J, Yuan T, Zhou T (2022) Investigations of teaching approach on fundamentals of fluid mechanics used by COMSOL. Automobile Applied Technology 47: 161-163. https://dx.doi.org/10.16638/j.cnki.1671-7988.2022.015.032
Liu JX, Yu F, Yan TH, He B, Guedes Soares C (2024) CFD-driven physics-informed generative adversarial networks for predicting AUV hydrodynamic performance. Ocean Engineering 313(Part 3): 119638. https://doi.org/10.1016/j.oceaneng.2024.119638
Liu HL, Huang TT (1998) Summary of DARPA SUBOFF experimental program data. Technical Report. Naval Surface Warfare Center Carderock Div Bethesda Md Hydromechanics. Bethesda MD
Lin Y, Guo J, Li HN, Zhu H, Huang H, Chen Y (2022) Study on the motion stability of the autonomous underwater helicopter. Journal of Marine Science Engineering 10(1): 60. https://doi.org/10.3390/jmse10010060
Lu Y, Yuan JP, Si QR, Tian D, Liu J (2023) Study on the optimal design of a shark-like shape auv based on the CFD method. Journal of Marine Science Engineering 11(10): 1869. https://doi.org/10.3390/jmse11101869
Ma XY, Zou L, Hu YJ, Yu Z, Gao Y, Wang X (2025) Experimental study on influencing factors of force change of slender submerged body under internal solitary wave. Ocean Engineering 316: 119897. https://doi.org/10.1016/j.oceaneng.2024.119897
Menter FR (1994) Two-equation eddy-viscosity turbulence models for engineering applications. AIAA Journal 32(8): 1598. https://doi.org/10.2514/3.12149
Menter FR, Langtry RB, Likki SR, Suzen YB, Huang PG, Völker S (2004) A correlation-based transition model using local variables—Part I: Model formulation. Journal of Turbomachinery 413-422. https://doi.org/10.1115/1.2184352
Mitra A, Panda JP, Warrior HV (2020) Experimental and numerical investigation of the hydrodynamic characteristics of autonomous underwater vehicles over sea-beds with complex topography. Ocean Engineering 198: 106978. http://dx.doi.org/10.1016/j.oceaneng.2020.106978
Mohamad R, Miralam M (2022) Combining CFD, ASE, and HEKF approaches to derive all of the hydrodynamic coefficients of an axisymmetric AUV. Proceedings of the Institution of Mechanical Engineers, Part M: Journal of Engineering for the Maritime Environment, 236(2): 474-492. https://doi.org/10.1177/14750902211034361
Phillips A, Furlong M, Turnock SR (2007) The use of computational fluid dynamics to determine the dynamic stability of an autonomous underwater vehicle. Available online: https://eprints.soton.ac.uk/48786/1/ABP_NUTTS.pdf (accessed on 26 July 2022)
Qin D, Huang Q, Pan G, Shi Y, Li F, Han P (2022) Numerical simulation of hydrodynamic and noise characteristics for a blended-wing-body underwater glider. Ocean Engineering 252: 111056. https://doi.org/10.1016/j.oceaneng.2022.111056
Roache PJ (1998) Verification and validation in computational science and engineering. Albuquerque, NM:Hermosa Publishers
Schultz MP (2007) Effects of coating roughness and biofouling on ship resistance and powering. Biofouling 23(5): 331-341. https://doi.org/10.1080/08927010701461974
Shadlaghani A, Mansoorzadeh S (2016) Calculation of linear damping coefficients by numerical simulation of steady state experiments. Journal of Applied Fluid Mechanics 9(2): 653-660. https://doi.org/10.18869/acadpub.jafm.68.225.24342
Shi DS (2021) Submarine operability. Beijing: National Defense Industry Press
Shih TH, Liou WW, Shabbir A (1995) A new k-ε eddy viscosity model for high Reynolds number turbulent flows. Computers & Fluids 24(3): 227-238. https://doi.org/10.1016/0045-7930(94)00032-T
Wang XH, Wang YH, Wang P, Niu W, Yang S, Luo C (2023) Sailing efficiency optimization and experimental validation of a Petrel long-range autonomous underwater vehicle. Ocean Engineering 281: 114604. https://doi.org/10.1016/j.oceaneng.2023.114604
Wang G, Wang Y, Yang M, Yang S (2024) Design and motion performance of a novel variable-area tail for underwater gliders. IEEE/ASME Transactions on Mechatronics 30(3): 2132-2143.

https://doi.org/10.1109/TMECH.2024.3424308

Wilcox DC (2006) Turbulence modeling for CFD. 2nd ed. La Cañada:DCW Industries, Inc

Wilcox DC (2008) Formulation of the k-ω Turbulence model revisited. AIAA Journal 46(11): 2823. https://doi.org/10.2514/1.36541

Wilmott P (1988) On the motion of a slender body submerged beneath surface waves. Journal of Ship Research 32(3): 208-219. https://doi.org/10.5957/jsr.1988.32.3.208

Wu J, Yang X, Xu S, Han X (2022) Numerical investigation on underwater towed system dynamics using a novel hydrodynamic model. Ocean Engineering 247: 110632. http://dx.doi.org/10.1016/j.oceaneng.2022.110632

Yang M, Wang YH, Yang SQ, Zhang L, Deng J (2021) Shape optimization of underwater glider based on approximate model technology. Applied Ocean Research 110: 102580. https://doi.org/10.1016/j.apor.2021.102580

Ye PC, Zhang H, Shi Y, Huang Q, Pan G, Qin D (2024) The blockage effect on resistance coefficients estimation for AUVs with different configurations in the towing tank. Journal of Marine Science and Engineering 12(9): 1532. https://doi.org/10.3390/jmse12091532

Zhang Z, Zhang X (2021) Course-keeping with roll damping control for ships using rudder and fin. Journal of Marine Science and Technology 26: 872-882. https://doi.org/10.1007/s00773-020-00779-6

Zhu CZ, Fu JL, Xiao DH, Wang J (2025) Nonlinear model order reduction of engineering turbulence using data-assisted neural networks. Computer Physics Communications 309: 109501. https://doi.org/10.1016/j.cpc.2025.109501

Zou L, Larsson L (2013) Computational fluid dynamics (CFD) prediction of bank effects including verification and validation. Journal of Marine Science and Technology 18: 310-323. https://doi.org/10.1007/s00773-012-0209-7